Effective Exploration of New 760°C-Capability Steels for Coal Energy

Final Scientific/Technical Report of DE-FE0008960

Funded by DOE National Energy Technology Laboratory (NETL)

by

The Ohio State University

Professors William Clark and Ji-Cheng Zhao

The Ohio State University

Department of Materials Science & Engineering

2041 College Road, Columbus, OH 43210

e-mails: clark.31@osu.edu; zhao.199@osu.edu

Date: September 17th, 2016

The Ohio State University

Final Scientific/Technical Report

Federal Agency: DOE National Energy Technology Laboratory (NETL)

Federal Grant Number: DE-FE0008960

Project Title: *Effective Exploration of New 760 ºC-Capability Steels for Coal Energy*

DUNS Number: 832127323

Project/Grant Period: 09/01/2012 to 08/31/2015 (no-cost extension to February 29, 2016)

Recipient Organization: The Ohio State University, Office of Sponsored Programs, 1960 Kenny Road, Columbus, OH 43210-1016, Attn: Anne Moffat.

PI Information: PI: Professor William Clark; co-PI: Professor Ji-Cheng Zhao
The Ohio State University, Department of Materials Science and Engineering, 476 Watts Hall, 2041 College Road, Columbus, OH 43210
Phone: 614-292-0575, Fax: 614-292-1537, Email: clark.31@osu.edu

OSU Business Point of Contact: Cynthia Korteweg, Ph: 614-292-4342, Email: korteweg.2@osu.edu

DOE Project Manager: Charles Miller, Phone: 412-386-5745, Email: charles.miller@netl.doe.gov

DOE Contract Specialist: Bethan Young, Phone: 412-386-4402, Email: bethan.young@netl.doe.gov

Submission Date: September 17, 2016.

Note: Professor Ji-Cheng (JC) Zhao was the original PI of this project. Since January 2014, he has taken a three-year assignment (85% appointment) under an Intergovernmental Personnel Act (IPA) agreement to serve as a Program Director at the Advanced Research Projects Agency – Energy (ARPA-E) of the U.S. Department of Energy. During Dr. Zhao's IPA appointment at ARPA-E, Prof. Clark kindly serves as the PI of this project while Prof. Zhao serves as a co-PI to satisfy the conflict of interest policies.

Table of Contents

List of abbreviations

AUSC: advanced ultrasupercritical (steam turbines)

CALPHAD: CALculation of PHAse Diagrams

EBSD: Electron backscatter diffraction

EDM: Electrical discharge machining

EPMA: Electron probe microanalysis

FIB: Focus ion beam

GTHT: Gradient temperature heat treated

HIP: Hot-isostatic-press

NSF: National Science Foundation

SADP: Selected area diffraction pattern

SEM: Scanning electron microscopy

TEM: Transmission electron microscopy

VHN: Vickers hardness number

Executive Summary

Cost effective and high performance alloys that are capable of operating at 760 °C or higher for extended periods of time under a very aggressive environment are critically required for the design and development of advanced ultrasupercritical (AUSC) boilers and steam turbines. Finely dispersed Laves phase precipitates have been shown by Takeyama and co-workers to be a viable strengthening mechanism in high temperature austenitic steels. There is currently no straightforward theory that can predict what other intermetallic phases can serve as potent precipitation-strengthening phases for steels; thus we employed a highly effective dual-anneal diffusion multiple (DADM) approach to screen for viable strengthening precipitates over a wide range of compositions. From the Fe-Co-Cr-Ni-Mo DADMs, the Fe-Cr-Mo based Chi phase was identified as a new strengthening phase for high temperature ferritic steels; and from the Fe-Mn-Cr-Nb-Ni-Mo-FeAl DADMs, the Laves phase was identified as a viable strengthening precipitate in Fe-Mn and Fe-Ni based austenitic steels.

After identification of viable strengthening phases from the DADMs that covered compositions in the basic ternary and quaternary systems, we employed computation thermodynamics to perform multicomponent alloy design and optimization. For the new the Chi-phase strengthened steels, we performed thermodynamic calculations to vary the volume fraction of the Chi phase and introduced Nb and carbon to promote the formation of stable carbides for grain size control during solution heat treatment. For the Fe-Ni-Mn based austenitic steels, we performed extensive parametric optimization of compositions in order to reduce the expensive Ni content, add Cr and Al for oxidation resistance, and balance the alloying contents (Ni, Mn, Cr, Al, Mo) to suppress the ferritic phase and promote the austenitic matrix phase.

Four steels (two ferritic + two austenitic) were designed and tested. The two Chi-phase strengthened ferritic steels exhibited excellent oxidation resistance and good creep-rupture strength at moderate temperatures, considering their ferritic matrix that usually results in lower creep resistance than austenitic steels. These steels showed brittleness and sample-to-sample variability in ductility. The low ductility might be due to the macro segregation during solidification or the significant grain growth during the solution heat treatments. We believe there is no inherent brittleness based on the chemistry of the steels. The creep-rupture performance of the steels is comparable to the 9Cr steels. Due to their ferritic matrix, the new Chi-phase strengthened ferritic steels may not be suited for the 760 °C AUSC applications, but they are very good candidates for intermediate temperature applications due to their outstanding oxidation resistance and high strength. Further study is required to find the source of low and highly variable ductility. We believe the compositions of the Chi-phase strengthened steels are not inherently brittle. The Chi-phase strengthened ferritic steels may also be excellent candidates for intermediate-temperature and room-temperature cast stainless steels, thus we highly recommend further investigations.

The two Mn-containing austenitic steels based on the Laves phase showed good ductility, excellent oxidation resistance (slightly inferior to the two ferritic steels) at high temperatures and moderate creep strength. The creep-strength of the two austenitic steels based on the Larson-Miller parameters is higher than that of the traditional 316 stainless steels, but lower than the alumina-forming alloys (AFAs) developed at Oak Ridge National Laboratories. We do not recommend high priority in further studying these compositions unless higher Cr alloys are required for hot-corrosion resistance.

1. Project background and objective

Cost effective and high performance materials that are capable of operating at 760 °C or higher for extended periods of time under a very aggressive environment are critically required for the design and development of advanced ultrasupercritical (AUSC) boilers and steam turbines. Current materials capable of operating at such temperatures are precipitation strengthened Ni-based alloys that are usually expensive and hard to process, as shown in Figure 1 [1,2,3,4,5,6]. It is highly desirable to develop low-cost steels that will be capable of operating at such temperatures and environment; however, most strengthening mechanisms for steels start to become inoperable at temperatures close to 760 °C. New mechanisms and/or new microstructures to strengthen steels at 760 °C or higher are highly sought after. In this case, the combinatorial/high-throughput methodologies are particularly suited in such a situation where a priori knowledge is not available concerning which phase or which microstructure will be a particularly potent strengthener.

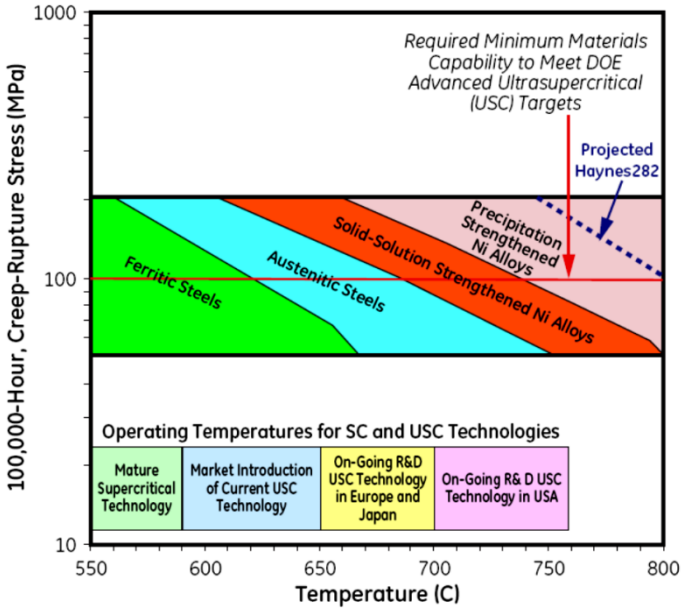

Figure 1 *Temperature capability of various engineering structural materials required for different coal energy systems according to Jiang et al. [1] (data from Viswanathan et al. [2-6]).*

The intermetallic Laves phase has been identified by Takeyama [7, 8, 9] and co-workers as strengthening precipitates in austenitic steels. A few steels have thus been developed with good mechanical strength at 700 °C using highly dispersed Fe_2Nb and carbides (Figure 2) with an alloy base composition of Fe-20Cr-30Ni-2Nb (at.%). Hot corrosion and oxidation resistance of the steel are achieved by high enough Cr content in the steels. Long before the work of Takeyama *et al.*, finely dispersed intermetallic phases, such as the sigma (σ) and mu (μ) phases, have already been used to strengthen several Ni-base alloys such as Hastelloy X [10] beyond the solid solution strengthening. These examples show that finely dispersed intermetallic phases are viable strengthening options for steels at high temperatures where other strengthening mechanisms start to wane. The key question then becomes how to most effectively look for the best intermetallic phases and associated microstructures to achieve the best high temperature

strength, while maintaining good oxidation and hot corrosion resistance as well as good ductility. Slow growth of finely dispersed intermetallic phases is also critical to the long-term strength stability of such steels.

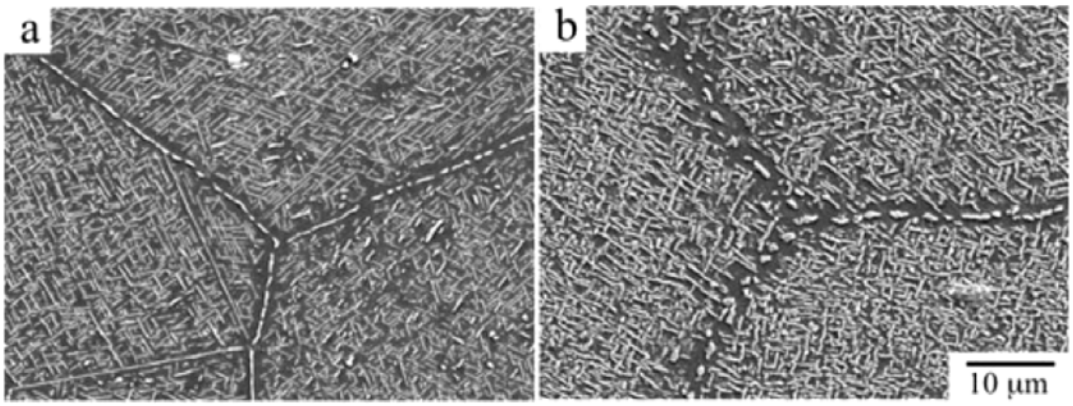

Figure 2 *Finely dispersed Laves phase in a Fe-20Cr-30Ni-2Nb (at.%) steel after a creep test at 700 °C and 120 MPa: (a) boron-doped steel, and (b) boron-free steel. The precipitates along the grain boundary are also critical to the creep resistance of the steels.*

The objective of this study is to identify new steels capable of operating at 760°C in the aggressive environments of AUSC boilers and steam turbines by exploring new compositions and new strengthening mechanisms/microstructures using high-throughput diffusion multiples and computational thermodynamics. A novel dual-anneal diffusion-multiple approach is used to effectively discover precipitate phases that are stable at 760 °C with a finely dispersed morphology. A high-temperature (e.g. 1200 ºC) anneal of diffusion multiples first creates wide composition regions of solid solutions and intermediate compounds, which is equivalent to making many alloy compositions simultaneously. A subsequent anneal at 760 ºC induces precipitate phases from the supersaturated solid solutions formed during the high-temperature anneal, which is equivalent to the heat treatment of many individual alloys at 760 ºC for a precipitation study. Each of the high-temperature annealed diffusion multiples can be sliced into several pieces for heat treatments at 760 ºC to obtain coarsening kinetics for various precipitate phases, thus achieving a very high efficiency. Nanoindentation and microhardness are performed at ambient temperature to map hardness across the solid solution and precipitation regions as a screening tool for high-strength compositions. Scanning electron microscopy (SEM) and localized transmission electron microscopy (TEM) sample extraction using focus ion beam (FIB) allow careful study of the structure of the precipitates.

Computational thermodynamics calculations using the CALPHAD (CALculation of PHAse Diagrams) approach are employed to extend the promising alloy compositions discovered from diffusion multiples to multicomponent systems by including other phases such as carbides and borides and by extrapolating from ternaries to multicomponent. A commercial database (TCFe5 from Thermo-Calc AB, Sweden) is used for the calculations.

Steel compositions with high Fe and Cr concentrations are the focus of this exploration because high Fe (instead of Ni) is important for cost reduction and high Cr is essential for oxidation and hot-corrosion resistance. Initial exploration will start with compositions developed

by Takeyama's group on Laves strengthened austenite stainless steels in the Fe-Cr-Ni-Al-based systems. Diffusion multiples will also be made to explore other potential precipitation phases and compositions. Both austenitic and ferritic steels are explored. Two Fe-Cr-Mo based ferritic steels with finely dispersed Chi phase precipitates discovered from a previous diffusion multiple experiment are used to test the high temperature properties of ferritic steels.

2. Identification of the intermetallic Chi phase as a viable high-temperature strengthening precipitate from dual-anneal diffusion multiples.

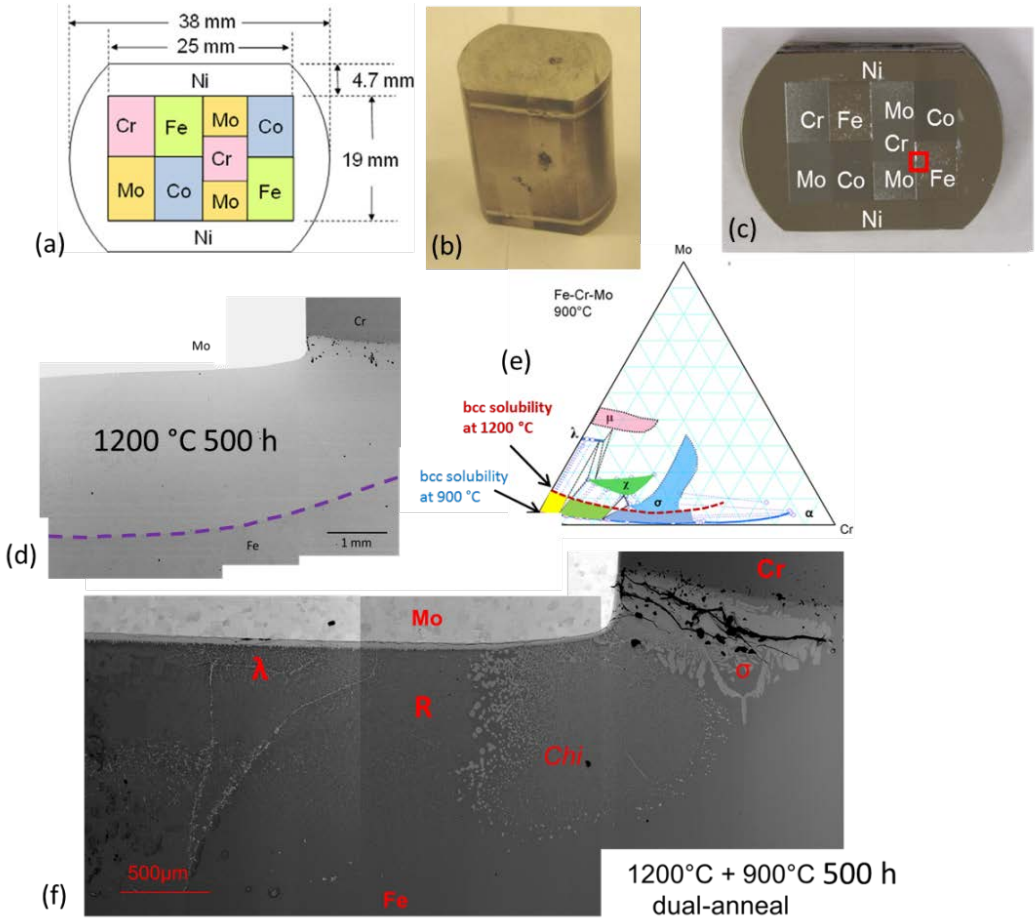

Figure 3 *A Fe-Co-Cr-Mo-Ni diffusion multiple and the Fe-Cr-Mo ternary system: (a) schematic geometry of the diffusion multiple; (b) photo after welding the top and bottom caps; (c) photo after heat treatments and metallography sample preparation; (d) SEM image of the Fe-Cr-Mo ternary junction after the first anneal at 1200 °C for 500 h and water quenched; (e) state-of-the-art isothermal section at 900 °C of the Fe-Cr-Mo phase diagram, the solubility limit of the bcc phase at 1200 °C was also sketched; and (e) SEM image of the Fe-Cr-Mo tri-junction region of the diffusion multiple after dual annealing at 900°C for another 500 h. The intermetallic precipitates were formed and labeled respectively.*

The Fe-Co-Cr-Mo-Ni diffusion multiples were made prior to this project under a National Science Foundation (NSF) project (NSF DMR-1237577). The intermetallic Chi phase was identified as a potential viable strengthening phase for high temperature ferritic steels. The diffusion multiple, as shown in Figure 3 [11], was made by inserting the pure metal pieces into a pure Ni piece with a 25x19 mm cut-out in the middle. Two pure Ni caps are electron beam welded onto the top and bottom of the Ni cartridge. After going through a hot-isostatic-press (HIP) run at 1200 °C and 200 MPa for 6 hours to achieve intimate interfacial contacts among the metal pieces, the diffusion multiple was annealed at 1200 °C for 500 h to promote interdiffusion and formation of wide range of compositions. One slice of this 1200 °C annealed diffusion multiple was further annealed at 900 °C for 500 h to promote precipitation of intermetallic phases from the supersaturated solid solutions.

The precipitation of the intermetallic Chi phase was studied in the Fe-Cr-Mo tri-junction region as shown in Figure 3. Figure 3(e) is a most-recent 900 °C isothermal section of the Fe-Cr-Mo system by Cao and Zhao [11]. The solubility limit of the bcc phase at 1200 °C was superimposed on this diagram for comparison. Due to the solubility differences between 1200 °C and 900 °C, the regions/compositions highlighted (light green for μ; yellow for Chi; gray for σ) in Figure 3(e) should have three different precipitates (μ, Chi, and σ phases with increasing Cr concentrations) after a second heat treatment at 900 °C for 500 h. There are also metastable precipitates as well. These precipitates can be clearly seen in the SEM image of Figure 3(f) with different morphologies: blocky σ, finely dispersed Chi, and finely dispersed μ. The Chi phase particles show different growth rate in the center of the Chi phase region, and along the Chi/R phase boundary. The concentration dependent growth rate indicates different phase transformation mechanism and kinetics. It is clear that the Chi phase particles in the center of the Chi phase field precipitate homogeneously and maintain as small particles even after 500 hours at 900 °C. This phase can thus potentially serve as a precipitation strengthener for ferritic steels for high-temperature applications.

Since the diffusion coefficients of elements in the bcc (ferrite) phase are usually significantly higher than those in the fcc (austenite) phase, it is generally expected that the high temperature creep strength of austenitic steels are better than those of ferritic steels. In this regard, it may be very critical to look for finely dispersed precipitates in the austenite phase as a base for high-temperature steel compositions. It is still worthwhile to take a careful look at a ferritic system to see how high the strength can be achieved through intermetallic phase precipitation strengthening since ferritic steels usually have better weldability. In this project, we designed two ferritic steels based on the intermetallic Chi phase as the precipitation strengthener based on the information we obtained from the diffusion multiples and computational thermodynamics.

3. Design, development and test of two ferritic steels based on the Chi phase.

3.a Design of two ferritic steels by computational thermodynamics.

The intermetallic Chi phase particles in the Fe-Cr-Mo system have uniform distribution at 900 °C even after 500 h, Figure 3. The distribution of this precipitate should be similar at 760 °C but the growth rate may be small enough to have very fine precipitates at this temperature of interest to AUSC steam turbines and boilers. Two ferritic steels were designed based on the Chi phase with the compositions carefully determined by computational thermodynamics. The Thermo-Calc™ software and a database of TCFe5 were used in the calculations. A small volume

fraction of MC carbides (basically NbC carbide) was included in each steel to pin the grain boundaries during thermal-mechanical processes to control the grain size for an optimal mechanical property. The designed and computed fraction of the each phase in the steels as a function of temperature is plotted as in Figure 4. Ferritic Steel #1 has a volume fraction of 40% of the Chi phase; while Ferritic Steel #2 has a reduced volume fraction of ~20% Chi phase.

The designed compositions of the steels were sent to Metalwerks Inc., Pennsylvania for casting and thermo-mechanical processing to produce steel plates. Figure 4(b) and 4(d) are the steel plates in "as-received" condition. Ingots of ~ 24-lb in weight were induction melted in vacuum and then hammer-forged to about 1" thick plates. During these processes, the steels show very good ductility at high temperatures and excellent oxidation resistance. Systematic cyclic oxidation resistance and precipitation study of these steels were conducted to find the best heat treatment conditions to achieve the optimum mechanical properties.

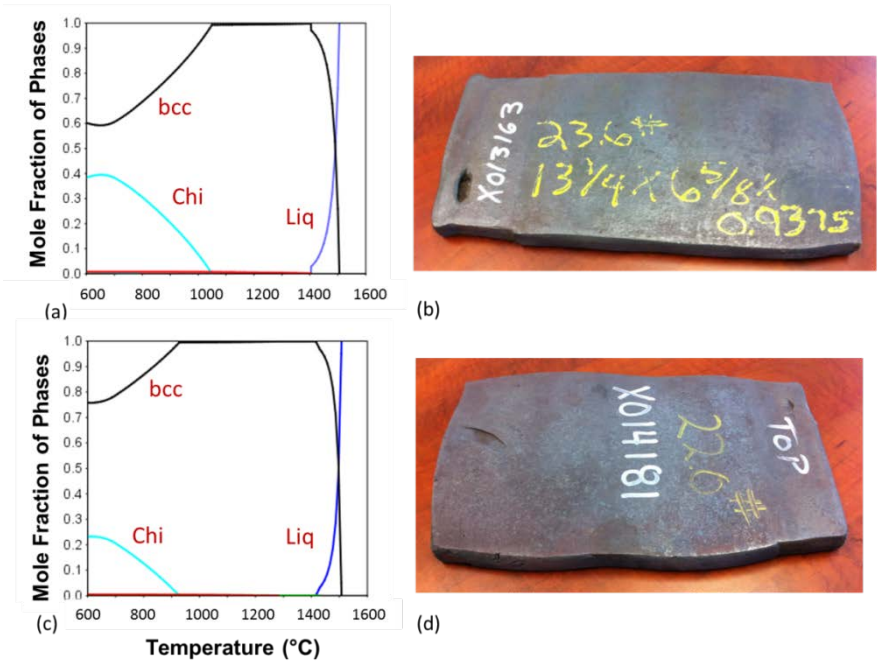

Figure 4 *(a) Mole fraction of each phase in Ferritic Steel #1 as a function of temperature, calculated by Thermo-Calc™ using the TCFe5 database. (b)"As-received" steel plate of Ferritic Steel #1. The dimension of the plate is 13'' x 6.7'' x 0.94''. (c) Mole fraction of phase calculation of Ferritic Steel #2, and (d)"As-received" steel plate of Ferritic Steel #2 with similar dimensions.*

3.b Solution heat treatment and optical microscopy of ferritic steels

Part of the plate of as-received Ferritic Steel #1 was sliced and cut into small pieces for the study for the optimum solutioning and precipitation annealing temperatures and time durations. Three undergraduate students were involved in this study as part of their senior design project under the guidance of the PIs and graduate students.

Since the two steels have similar compositions, the best solutioning precipitation annealing

recipe should be similar. Ferritic Steel #1 is taken as an example for the study. The solution heat treatments have been performed at temperatures from 1050 ºC to 1200 ºC at several time durations per temperature. It was found that a solution treatment at 1200 ºC for at least 6 h can dissolve most of the precipitates formed during the ingot casting and upsetting (hammer-forging). We thus defined the optimum solution condition to be 1200 ºC for 6 to 8 h. Figure 5 shows the microstructure of Ferritic Steel #1 revealed by optical microscopy. The etchant used for this steel was a solution of 40 volumes of HCl + 30 HNO_3 + 40 H_2O.

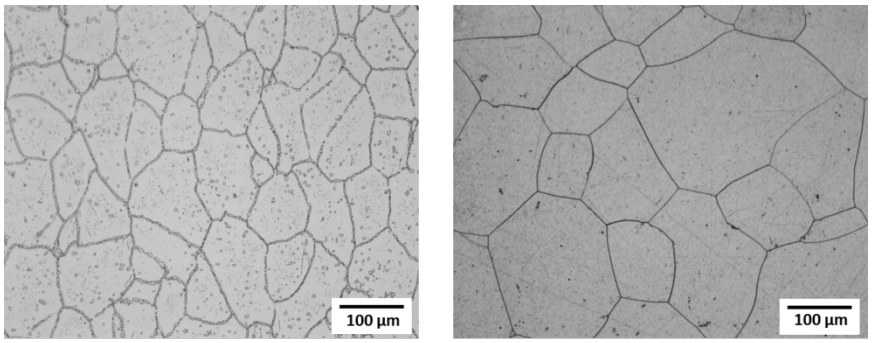

Figure 5 *Optical images of Ferritic Steel #1 in "as-received" condition (a) and after solutioning heat treatment at 1200 °C for 7.5 h (b), showing the dissolution of 2nd phase precipitates inside the grains and along the grain boundaries as a result of the solution heat treatment.*

3.c Gradient temperature heat treatment technique for effective screening of the optimal precipitation heat treatment temperature

After determining the solution treatment condition, a series of precipitation heat treatments were performed at temperatures from 500 ºC to 1000 ºC. Uniformly dispersed Chi-phase precipitates were observed, including uniform distributions along the grain boundaries. To avoid the tedious individual heat treatment, grinding/polishing, and hardness testing of the individual samples, we designed a high-throughput experiment by heat treating the steel in a gradient temperature environment. Vicker's hardness test was performed before and after the heat treatment to show the relationship between the hardness increase and the heat treatment temperature. One gradient treatment is from ~520 °C to 920 °C and the other from ~760 °C to ~1010 °C.

A steel bar was solutionized at 1200 °C and then quenched into ambient temperature water. It was first polished down to a 1-micron finish and hardness measurements using microindentation was performed across the length of the sample. Nine holes spaced 0.5 inch apart were drilled halfway into the sample and nine type-K thermocouples were fixed into the holes, as shown in Figure 6. Once the thermocouples were attached, the bar was placed in a tube furnace at the end of the tube as shown in Figure 7 with one end of the furnace open to create a temperature gradient. The sample was annealed for 10 hours. The temperature from each thermocouple remained very stable throughout the annealing process, ranging from 518°C at one end of the bar to 920°C on the other end. Several trials were performed before the experiment to make sure the desired temperature range could be achieved. Figure 8 shows the exact temperature gradient of the bar from the readings of the thermocouples. The data lines in Figure 8 are actually 4 lines

stacked on each other and we can see the actual variation at each data point is very small (< ±3 °C). After heat treatment, the thermocouples were removed from the bar and the oxide layer was removed from the sample surface by grinding. The sample was polished and Vicker's hardness test was performed again. The bar was then etched and images (both optical and SEM) were captured at the locations adjacent to each of the thermocouples to analyze the microstructure at each temperature.

Figure 6 *Sample for a gradient temperature precipitation heat treatment. Nine holes drilled on a steel bar with 0.5-inch spacing. Nine individual type-K thermocouples were attached to the sample and bent towards one direction for attachment to the temperature measurement unit.*

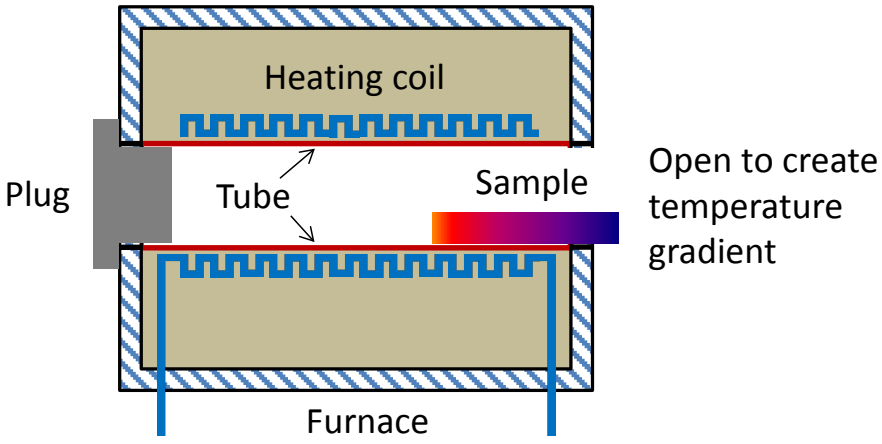

Figure 7 *Sample setup of the steel bar in a tube furnace to create a temperature gradient.*

Figure 8 shows the exact temperature of each thermocouple reading. The temperature at locations between the thermocouples was assumed linearly distributed and interpolated in Figure 8. At 0 mm, nearest to the open end of the tube, the temperature was at 518 °C. At the opposite end, 100 mm marks the hottest location of 920 °C. Vickers hardness test was conducted on the bar before the annealing to produce the "Pre-Heat Treat" dataset in Figure 9. Then, the bar was

heat treated for 10 h near the open-end of a tube furnace with a temperature gradient. The bar was polished and hardness test was performed to obtain the "Post-Heat Treatment" dataset. Overall, the hardness increases after the precipitation annealing, showing precipitation strengthening. At the location of about 18 mm from the 1st thermocouple and the temperature is extrapolated from Figure 8 to be 620 °C), there is a peak in the measured microhardness, showing the optimum precipitation annealing temperature (for 10 h annealing).

Through the gradient temperature experiment, we were able to find a precipitation heat treatment condition that produces a Vickers hardness number (VHN) of 370 as compared to 270 VHN prior to the precipitation heat treatment. The hardness of this new steel is comparable to some martensitic steels, and is significantly better than the best of pearlite steels. We expect our steels will be able to keep good strength at high temperatures at which both pearlite steels and martensitic steels cannot maintain their high strength.

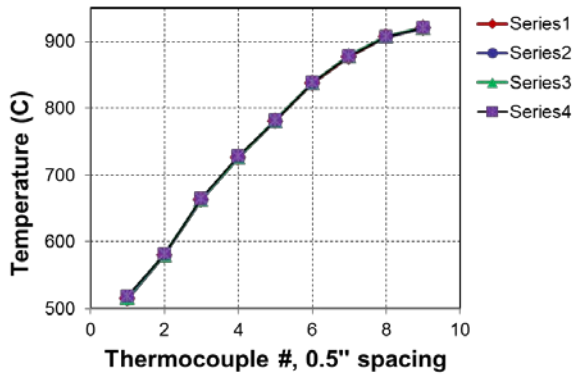

Figure 8 *Temperature recording at each thermocouple location of the steel bar.*

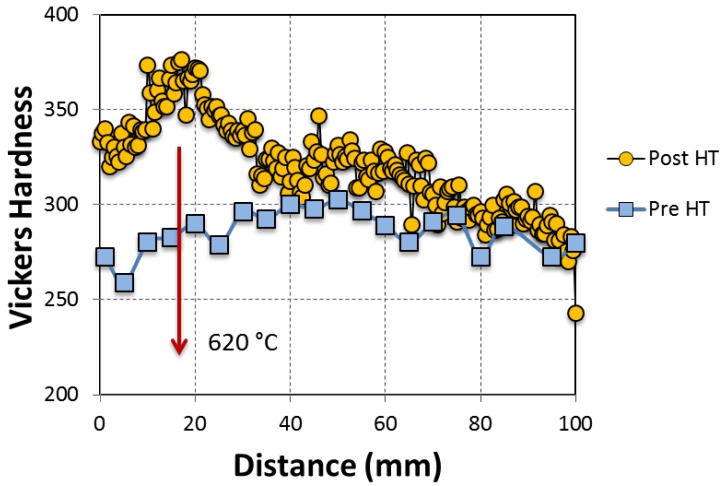

Figure 9 *Vickers hardness measurement as a function of location with regard to the low-temperature end of the steel bar before and after the gradient temperature experiment.*

To further understand the phase transformation kinetics and precipitation morphology of the Chi phase in the steel, we performed high-resolution SEM analysis of the steel to study the microstructure. Information regarding the phase transformation kinetics at different temperatures of this steel can be obtained efficiently from the gradient temperature heat treated (GTHT) steel bar in a temperature range from 518 °C to 920 °C. To get high-quality SEM images with clear precipitates/matrix interfaces, we found it is critical to obtain an excellent sample surface prior to SEM. Usually it is achieved by placing the steel specimen in a vibration polisher for at least overnight.

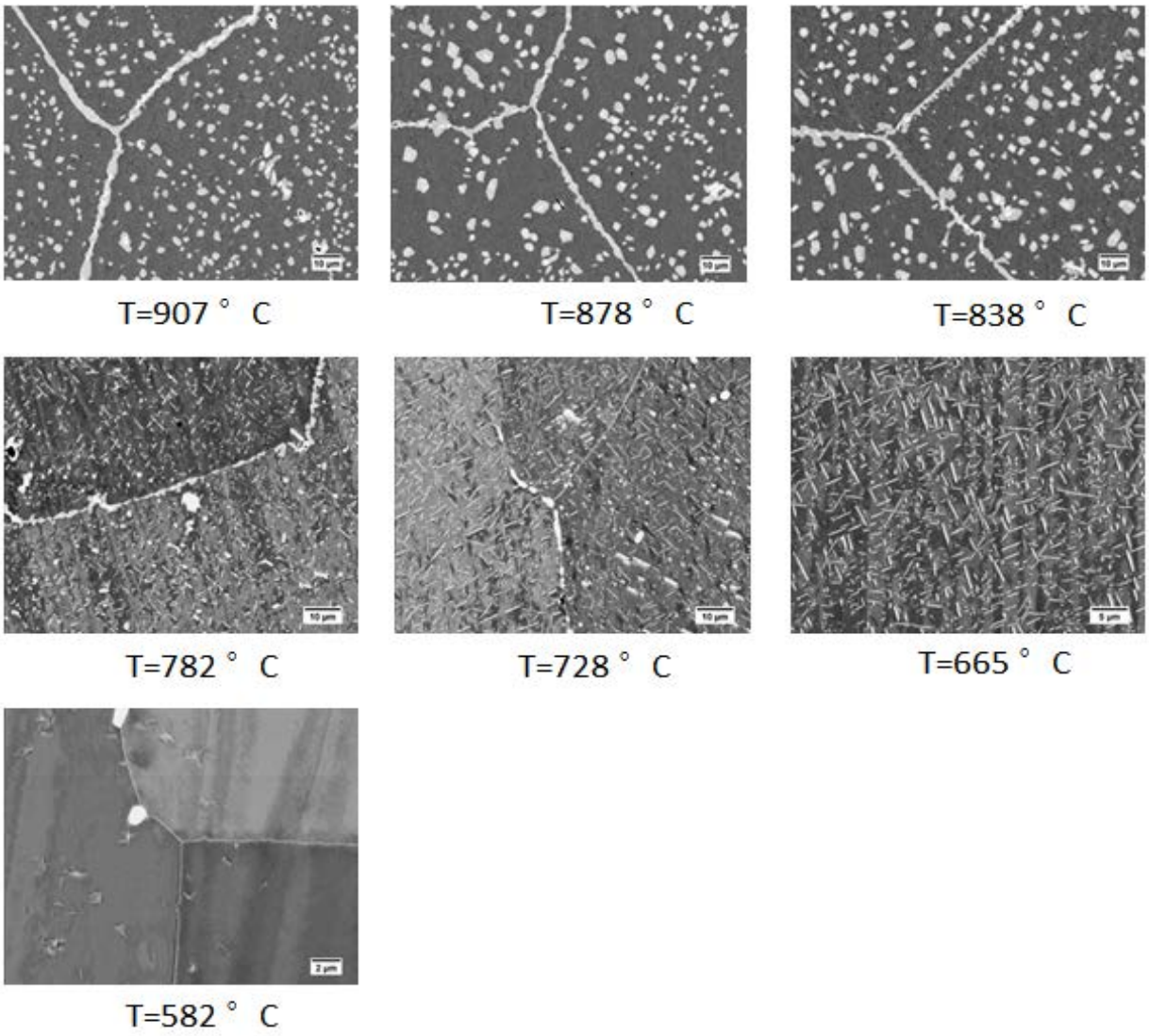

Figure 10 *High resolution SEM images taken at different locations on the GTHT steel bar. Thin plate-like precipitate started to emerge at ~785 °C and their volume fraction became higher as the temperature decreased towards 665 °C. At 582 °C, only a few precipitates were found due to the sluggish kinetics at this temperature.*

The high-resolution SEM images taken at several locations near the thermocouples were shown in Figure 10. In the temperature range from 907 °C to 838 °C, the precipitates were mainly in the form of the Chi phase with a small amount of NbC carbides (the structural analysis of these precipitates by either electron backscatter diffraction (EBSD) in SEM or selected area diffraction patterns (SADP) in TEM will be discussed in later). The Chi precipitates show a equiaxed shape and they precipitated both along the grain boundaries and inside the grains. As the temperature decreased from 907 °C to 838 °C (Figure 11), the volume fraction of the Chi phase increased, which is consistent with thermodynamic calculations; on the other hand, the mean radius and inter-particle spacing decreased, which improved the strength of the steel. Beginning from the temperature of 782 °C, a plate-like phase, in addition to the spherical Chi phase, was formed in the steel. There were still a few Chi phase particles, but the volume fraction was far less than the plate-like phase. The plate-like phase shows a 6-fold symmetry, from which it is deduced to be the hexagonal Laves phase as indicated by the diffraction study in TEM. The Laves phase did not preferably precipitate along the grain boundaries but mainly inside the grains with a uniform distribution in the matrix. At temperature 582 °C, only a small amount of fine particles was seen, which is due to the sluggish kinetics at low temperature such that the precipitates do not have enough time to grow.

3.d EBSD phase identification of Ferritic Steel #1 at the location of 838 °C of the GTHT sample.

EBSD in SEM is now a well-established technique for crystallographic analysis of bulk material samples and it can be used to verify the crystal structures of crystalline phases. The major advantage of EBSD is its ability to rapidly analyze large areas of regular metallographic samples without the need to prepare thin foils as required for TEM analysis. However, regular EBSD is hard to be applied to sub-micrometer sized phases without the use of the transmission Kikuchi diffraction (i.e., EBSD in transmission mode).

In the GTHT steel bar, we found the mean radius and morphology of the precipitates in the steel change gradually with decreasing aging temperature from 920 °C to 518 °C. Based on the correlation of the morphology and Thermo-Calc^{TM} calculations, we anticipate the majority of the spherical precipitates are the intermetallic Chi phase (with some NbC on the grain boundary) when the temperature is high than 782 °C, and the majority of the plate-like precipitates are the Laves phase which emerges in the lower temperature regime. There might also be some metastable intermediate phases. EBSD or TEM based crystallographic analysis is required to provide phase identification information of these phases.

Since the diameter of the precipitates in the high temperature regime of the GTHT steel bar is on the order of a few microns, EBSD was employed for the phase identification. In this case, since the overall composition of the steel is already known, the precipitate would very likely be one of the intermetallic phases in the Fe-Cr-Mo ternary system, i.e., the μ, Chi, Laves, and R phases. All the crystallographic information on these intermetallic phases is used as possible candidates for phase verification.

The steel specimen was prepared by standard metallography sample preparation procedures. The final polishing step was on a vibration polisher using 0.05 μm non-crystalline colloidal silica

for a few hours. EBSD was then carried out using a FEI XL-30 with patterns detected using software TSL OIM 7 (FEI is a microscope manufacturer (http://www.fei.com); TSL is a brand name of EDAX Inc. (http://www.edax.com); and OIM stands for orientation imaging microscopy). The EBSD patterns of the specific precipitates were collected by the microscope and then compared with the simulated patterns (Kikuchi bands) generated in the software from known crystal structures in the database. Once a match is found, the crystal structure is positively identified. To get reliable analysis results, an indexed EBSD pattern usually needs have a confidence index higher than 0.2. All the crystal structure information of the candidate phases were collected from literature and imported into the OIM software. The intermetallic NbC, and the Chi phases were identified, as shown in Figure 12 and Figure 13.

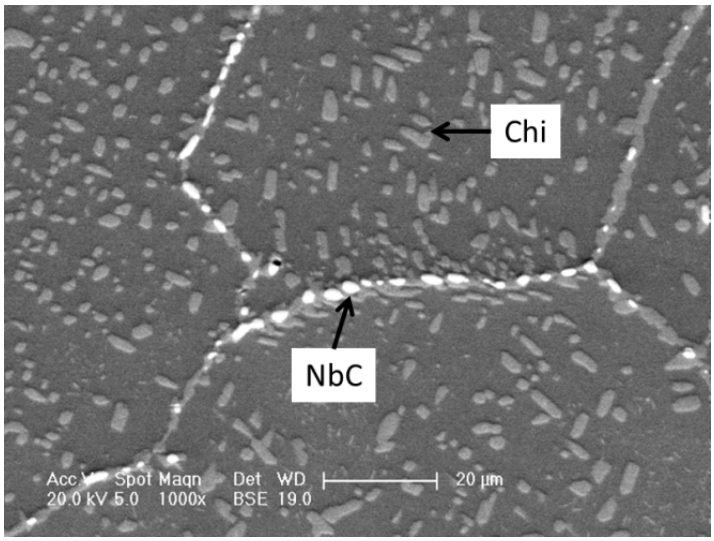

Figure 11 *SEM backscattered electron image shows two distinct phases in Ferritic Steel #1 at the 838 °C location in the GTHT steel bar (equivalent to 838 °C 10 h precipitation heat treatment.*

The crystallographic information of the NbC phase was reported in [12]. It has an fcc crystal structure with a space group of Fm-3m with a lattice constant of 4.47 Å. It has a prototype structure of NaCl. The NbC is intentionally added into this steel as grain boundary strengthener which also pins the boundary so the average grain size could be controlled. EBSD patterns were collected on a few distinct NbC precipitates with different orientation to get the crystallographic information, as shown in Figure 12.

The Chi phase is a Fe-Cr-Mo ternary intermetallic phase. It has a body-center cubic (bcc) crystal structure (alpha-Mn prototype structure), with a space group of $I4\bar{3}m$ and a lattice constant of around 8.92 Å. Detailed crystal structure information of this phase was in Ref. [13]. Again, EBSD was employed to verify the crystallographic information of this phase.

EBSD diffraction pattern has successfully been applied to verify the crystallographic information of the NbC and the intermetallic Chi phase. Since the location in this study is still in the higher temperature regime where the precipitates are relatively large, our future work is to extend this method to the lower temperature regime (where the precipitates are smaller) of the GTHT steel sample to see if the precipitates are still able to be resolved and indexed correctly.

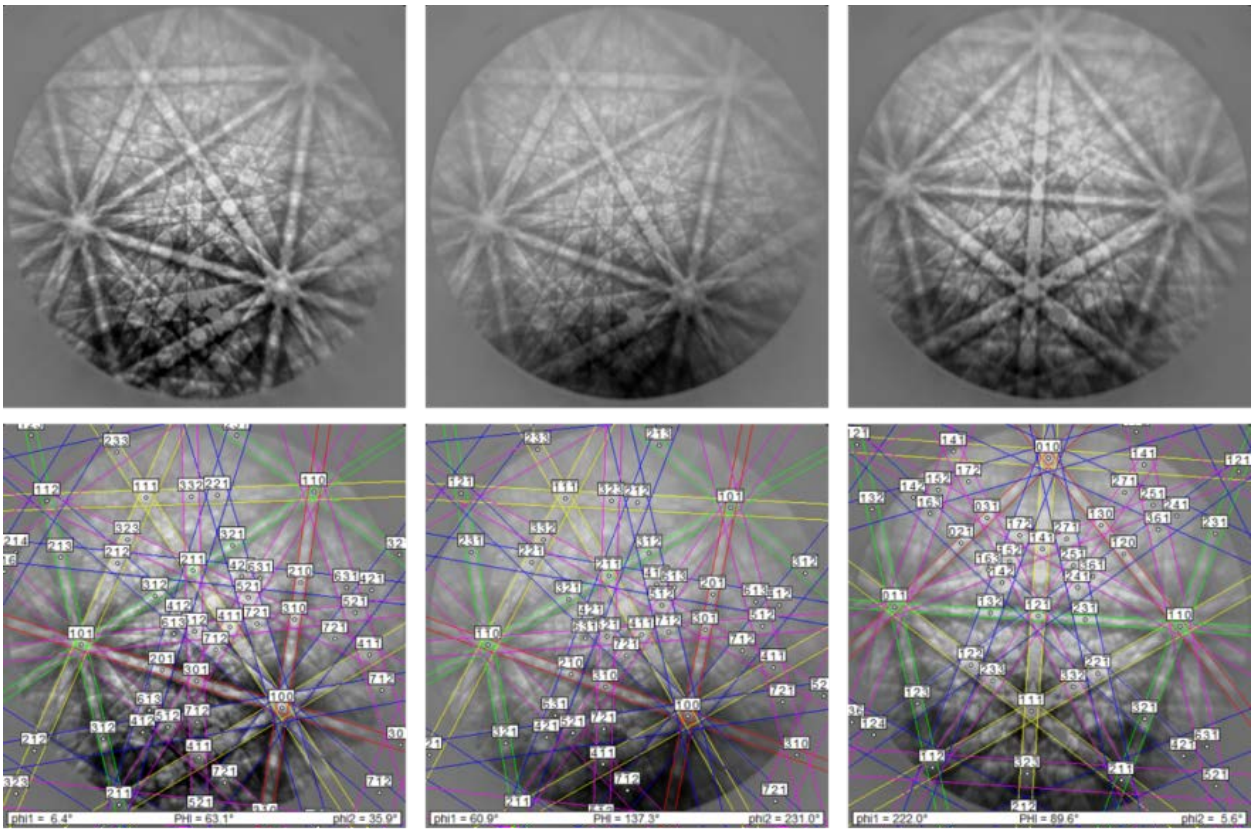

Figure 12 *EBSD patterns of the NbC phase with 3 different orientations. Pictures on the top are the raw experimental patterns. Pictures on the bottom are the indexed patterns with simulated pattern overlay. The average confidence index is 0.69.*

3.e TEM phase identification of the ferritic steel at the location of 760 °C in the GTHT sample.

Figure 14(a) shows the SEM image of the microstructure of the ferritic steel aged at 760 °C for 10 h and two distinct precipitates were observed based on their morphology. One is plate-like and the other is close to spherical/equiaxed but small. Since we have one sample with location specific microstructures, localized sample extraction by FIB is suited in this study for the TEM sample preparation. TEM foil was extracted to contain both precipitates using FIB technique and TEM SADPs were collected on both kinds of precipitates.

The bulky precipitate was found to be equiaxed in shape, as indicated with a blue circle in Figure 14(c). Series of SADPs were collected along a few zone axes following the transmission Kikuchi lines. Software simulations were also made using the SingleCrystal module in the CrystalMaker software. Since the precipitate particles are relatively large in this case, so SADPs using the smallest selected area aperture was actually a single-crystal diffraction. The diffraction patterns were shown in Figure 15 and it was identified as the Chi phase.

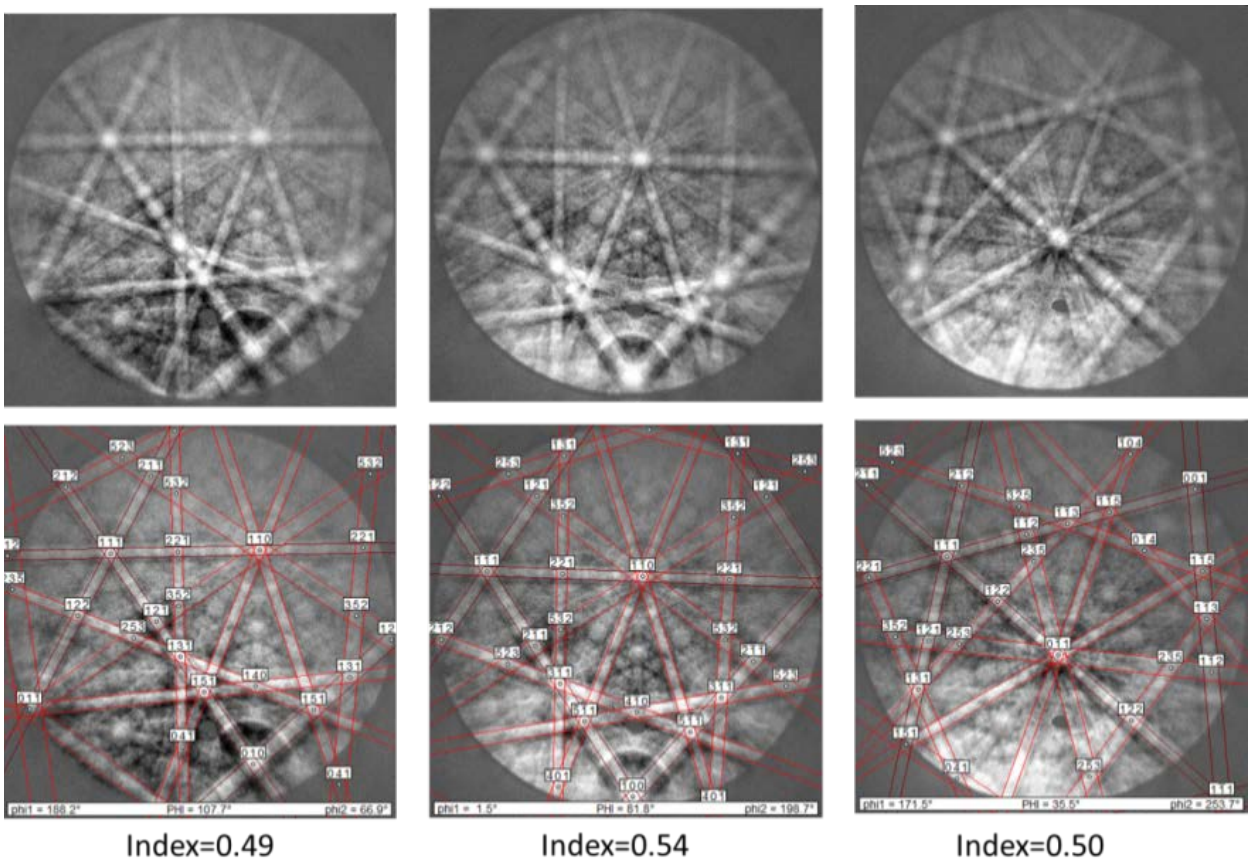

Figure 13 *EBSD patterns of the intermetallic Chi phase with 3 different orientations. Pictures on the top are the raw experimental patterns. Pictures on the bottom are the indexed patterns from the software with simulated pattern overlay. The average confidence index is 0.51.*

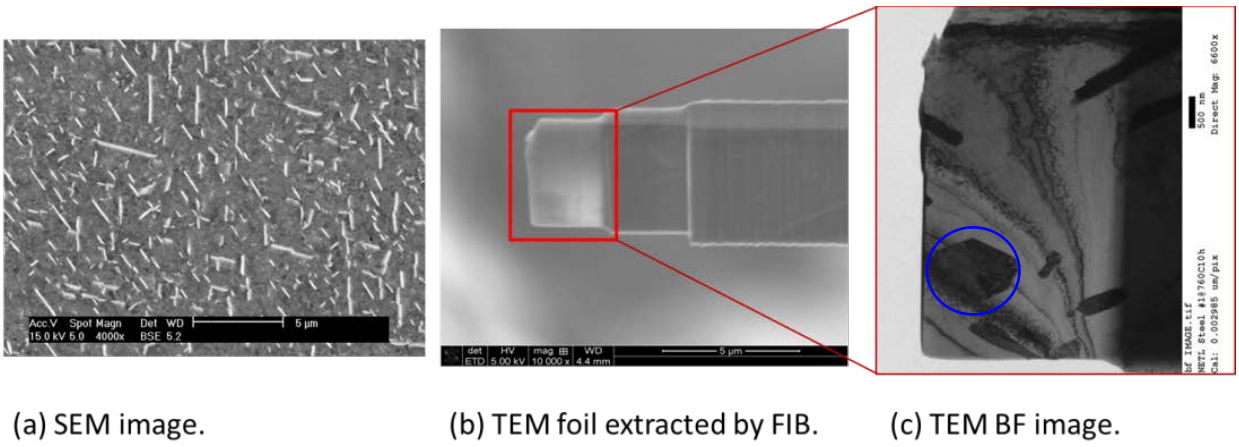

Figure 14 *(a) SEM image of the steel aged at 760 °C for 10 h; (b) Extracted FIB foil; (c) TEM bright field (BF) image showing the two distinct precipitates in the steel.*

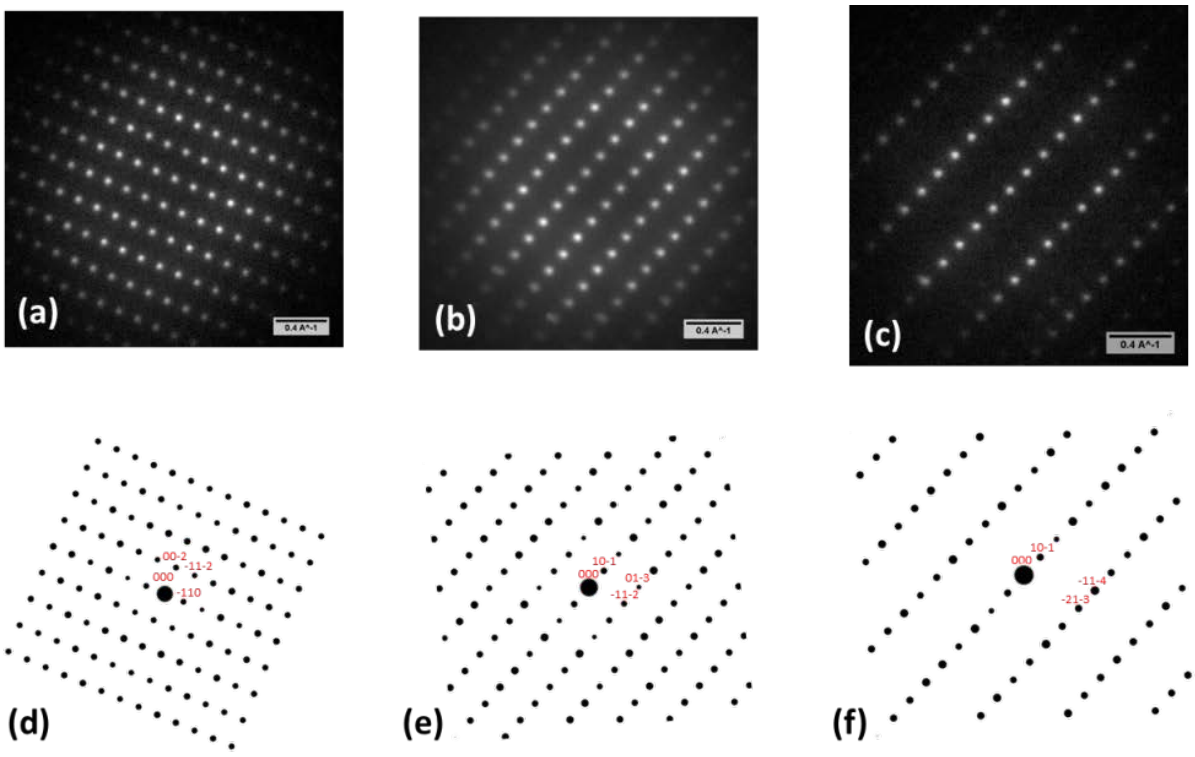

Figure 15 *Experimental diffraction patterns on the precipitate and the corresponding simulated key diagrams. (a,d) Chi phase on zone <110>; (b,e) Chi phase on zone <131>; (c-f) Chi phase on zone <151>.*

The other precipitate in this steel sample was found to have a plate-like shape, as shown in both the SEM and TEM images in Figure 14. It is obviously not the Chi phase. Detailed structural analysis by TEM diffraction confirmed this precipitate as the Laves phase, Figure 16.

It seems that the steel has different precipitates at temperatures below 760 °C, which deviated from the results of Thermo-Calc calculation. This could be due to the inaccuracy of the thermodynamic database at lower temperatures since the thermodynamic parameters are extrapolated from high-temperature assessments. It may also be the case that the Laves phase is actually a metastable phase which precipitated out first prior to the Chi phase.

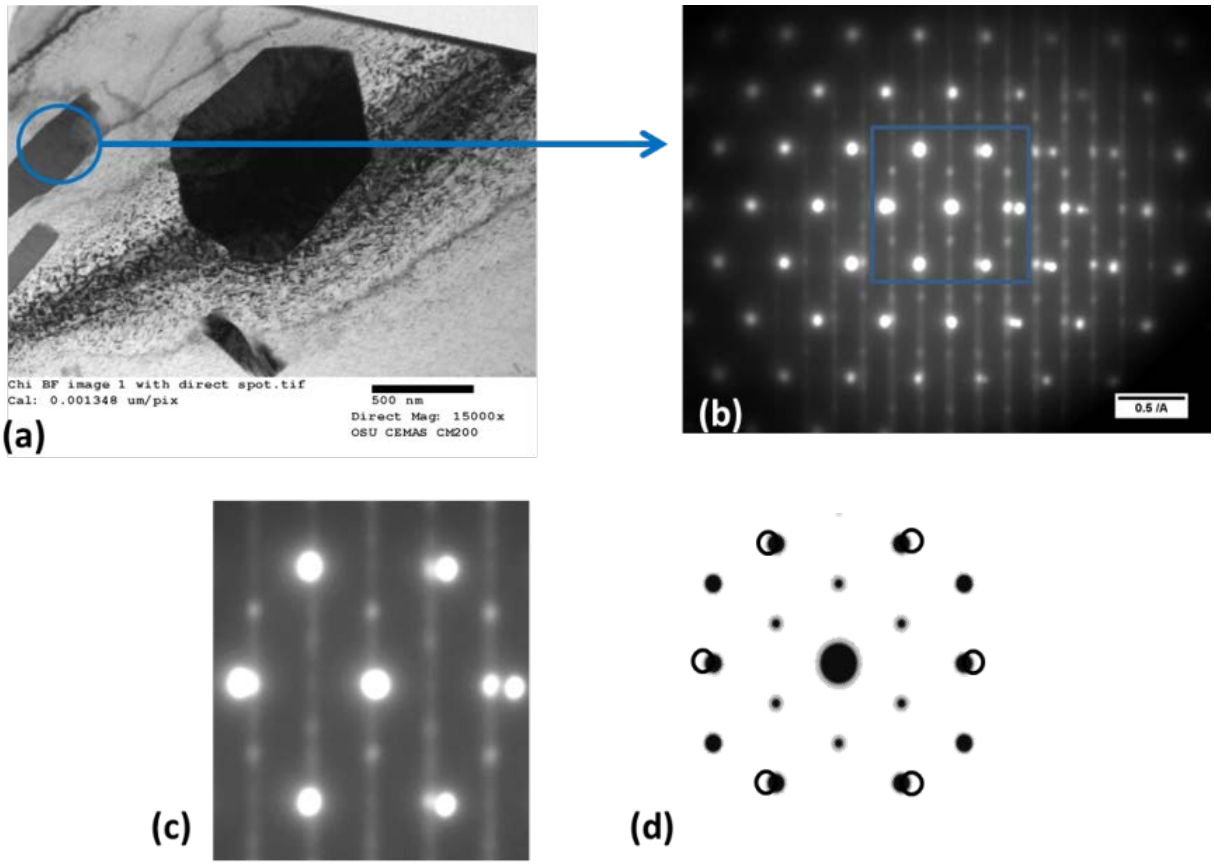

Figure 16 *SADP analysis of the needle-like precipitate in the ferritic steel. (a) TEM BF image showing both the needle-like phase and the Chi phase. (b) SADP of the needle-like phase. (c) cropped area of the diffraction pattern near the center direct beam, and (d) simulated diffraction patterns. The bright spots are from the bcc matrix along <111> direction, the dark spots are from the Laves precipitates along <001> direction.*

3.f Mechanical property tests.

1. Room-temperature tensile test (Ferritic Steel #1)

We first heat treated the raw steel bar at 1200 °C for 9 h and then 620 °C for another 12 h for the Chi-phase to precipitate from the matrix. Water quench was performed after every heat treatment to retain the high-temperature microstructures. After the heat treatment, tensile sample bars were made according the ASTM standards E8/E8M-11 (see Figure 17). The strain rate of the test is 2.5×10^{-4} s^{-1}. The strain-stress curve, Figure 18, shows the steel failed before the yield point, indicating very brittle fracture. The brittleness may be due to the high volume fraction of the Chi phase in the alloy.

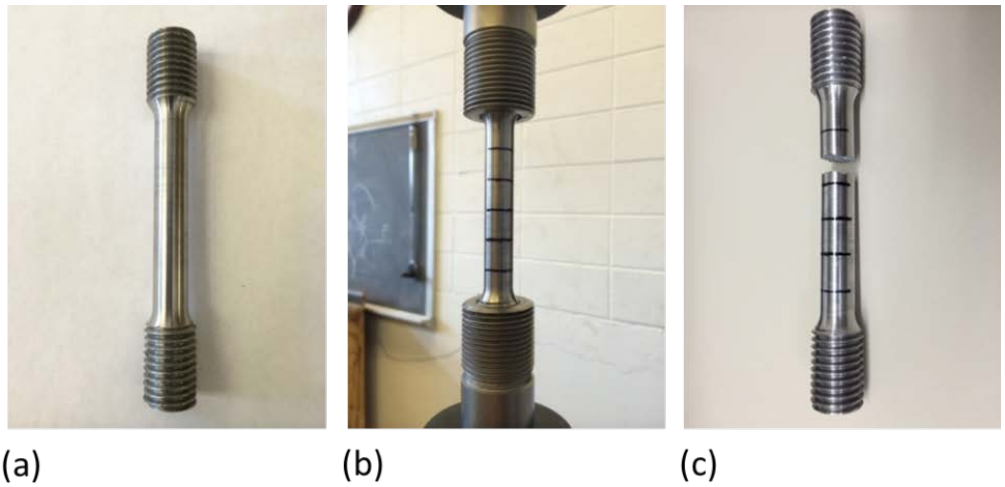

Figure 17 *(a) Room temperature tensile test sample dimension; (b) Sample on the test machine; and (c) Sample after the test was complete.*

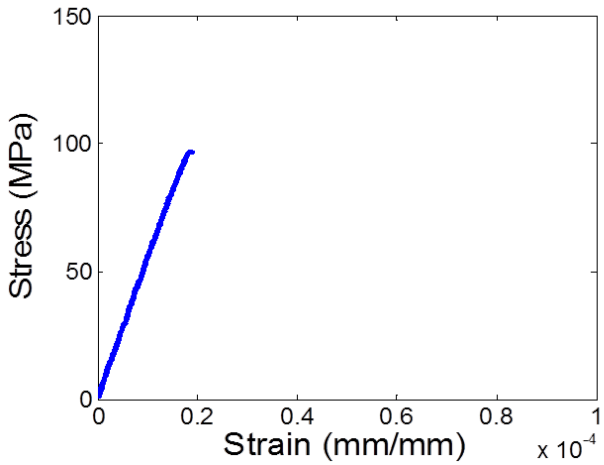

Figure 18 *Stress-Strain curve of the tensile test at room temperature.*

2. Tensile test at 550 °C for Ferritic Steel #1

Tensile test at 550 °C was also performed using a test specimen according to ASTM standards, Figures 19 and 20. The test was done using a cube furnace. The sample was soaked at temperature for 30 min prior to the actual test. The stress-strain curve shows that the yield strength (σ_ε = 0.2%) of this steel is around 680 MPa at 550 °C, and it is still very brittle. The strain rate of the test is 2.5×10^{-4} s^{-1}.

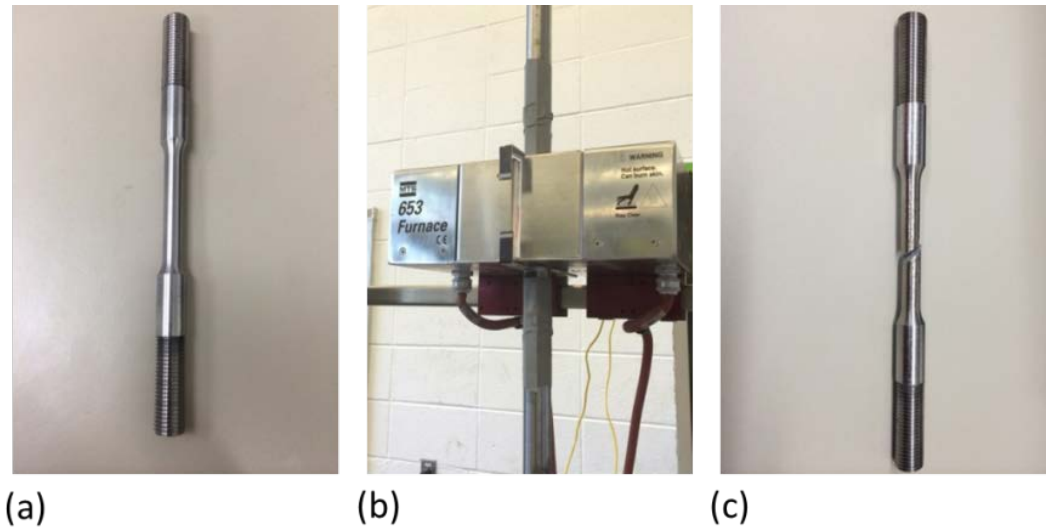

Figure 19 *(a) Tensile test specimen at 550 °C with a diameter of 0.25"at the reduced section area; (b) Specimen was placed on the test frame equipped with cube furnaces; and (c) Specimen after the test.*

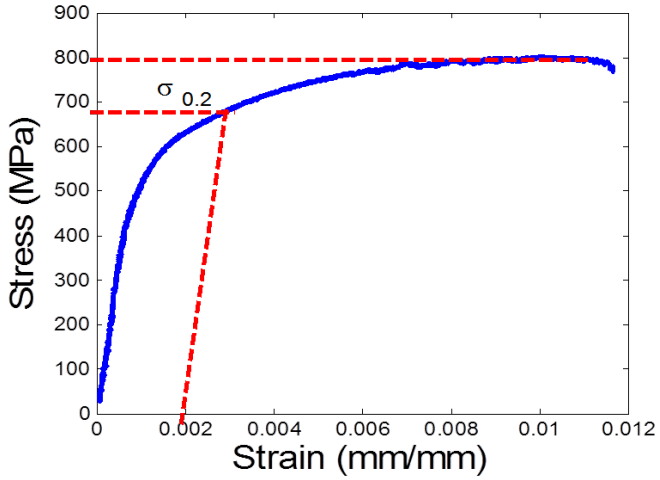

Figure 20 *Stress-strain curve of Ferritic Steel #1 tested at 550 °C.*

3. Creep test at 550 °C for Ferritic Steel #1

Besides the tensile test at 550 °C, we also performed the creep test at this temperature with a constant stress of 350 MPa. The calculated Larson-Miller parameter of the current test result was compared with one of the traditional high-temperature ferritic steels (Fe-9Cr-1Mo-V) in literature, as shown in Figure 21.

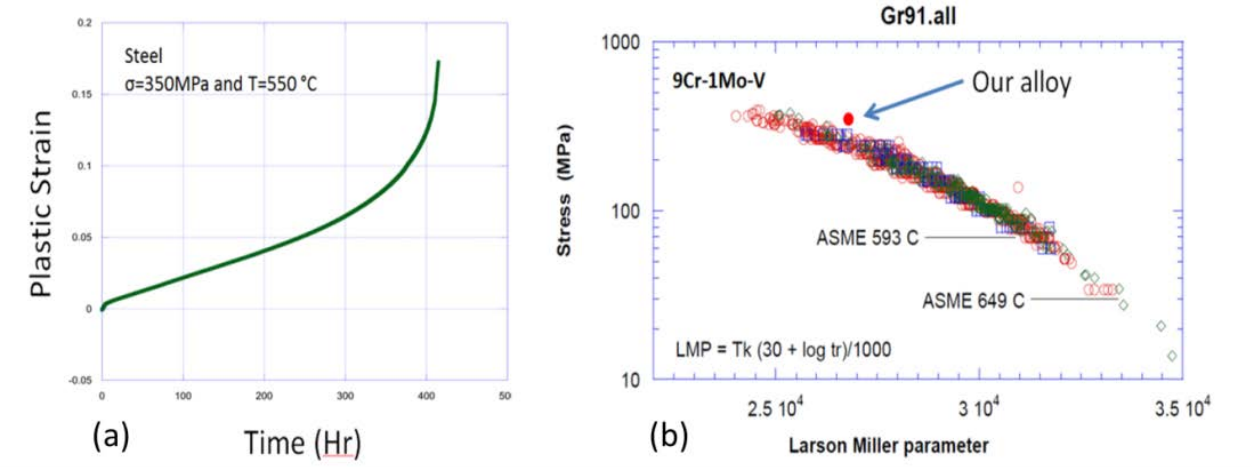

Figure 21 *(a) Creep test curve of the Chi steel with a stress of 350 MPa at 550 °C; (b) Comparison of the calculated Larson-Miller parameter with another high temperature ferritic steel Fe-9Cr-1Mo-V in the literature. Our alloy performs similar to the 9Cr steel. The literature data is from a CRADA final report by Michael Gold (http://web.ornl.gov/~webworks/cppr/y2001/rpt/119036.pdf).*

4. Room temperature tensile test of the "as-received" Ferritic Steel #2

Two samples were cut from the steel plate from the bottom and machined to tensile specimens per the ASTM standard. The stain-stress curve is shown in Figure 22. Though cut from the same location, the two specimens showed different modes of failure. The first sample showed an elongation of about 15%, while the other sample showed only about 2%. The 0.2% yield strength for the steel in "as-received" condition is 410 MPa. The strain rate of the test is 2.5×10^{-4} s^{-1}.

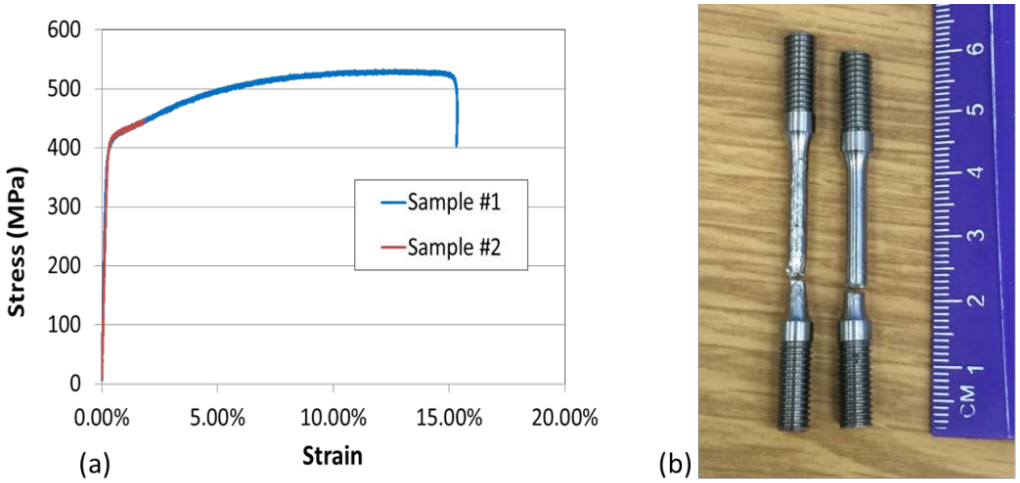

Figure 22 *Tensile test of Ferritic Steel # 2 in "as-received" condition (induction melted and then hammer forged).*

5. Tensile test at room temperature of the 1200 °C solution treated Ferrite Steel #2

Similar as what was performed for tensile tests of the steel in the "as-received" condition, we performed a tensile test of the steel after solution heat treated at 1200 °C for 8 h without the precipitation annealing. Again, two specimens were cut from the same location in the bottom of the steel plate and machined per ASTM standard. The strain rate of the test is $2.5x10^{-4}$ s^{-1}.

The stress-strain curves in Figure 23 show the ductility of the steel after solutionization heat treatment at 1200 °C for 8 h is similar to that before the treatment. The yield strength somehow increased from 410 MPa to 510 MPa. Significant necking was observed on the tested samples, which indicates good ductility after the solutioning at 1200 °C.

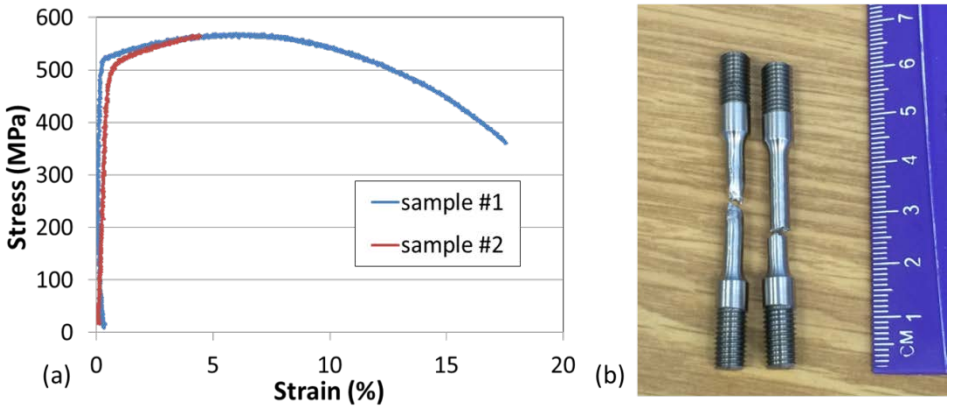

Figure 23 *Room temperature tensile tests of Ferritic Steel #2 after solutionization at 1200 °C for 8 h. The strain rate of the test is* $2.5x10^{-4}$ s^{-1}.

6. Tensile test after aging heat treatment of 1200 °C 8 h and 600 °C 12 h of Ferritic Steel #2.

Figure 24 shows the results of tensile tests of Ferritic Steel #2 that underwent the heat treatment at 1200 °C 8 h and an aging treatment at 600 °C for 12 h. The yield strength of the steel after the aging treatment at 600 °C is around 540 MPa and the ductility was decreased to only 6%. The Chi phase precipitates increased both the yield strength and the ultimate tensile strength significantly, but the side effect is the reduced ductility.

The ductility of this steel has shown tremendous variation from sample to sample. The reason might be due to the micro-segregation of the ingot after casting and hammer forging due to the slow kinetics of the heavy elements such as Mo and Nb in the steel. There is no inherent brittleness of these compositions, but the volume fraction of the Chi phase may need to be further decreased to increase the room temperature ductility of the ferritic steels based on the Chi phase strengthening.

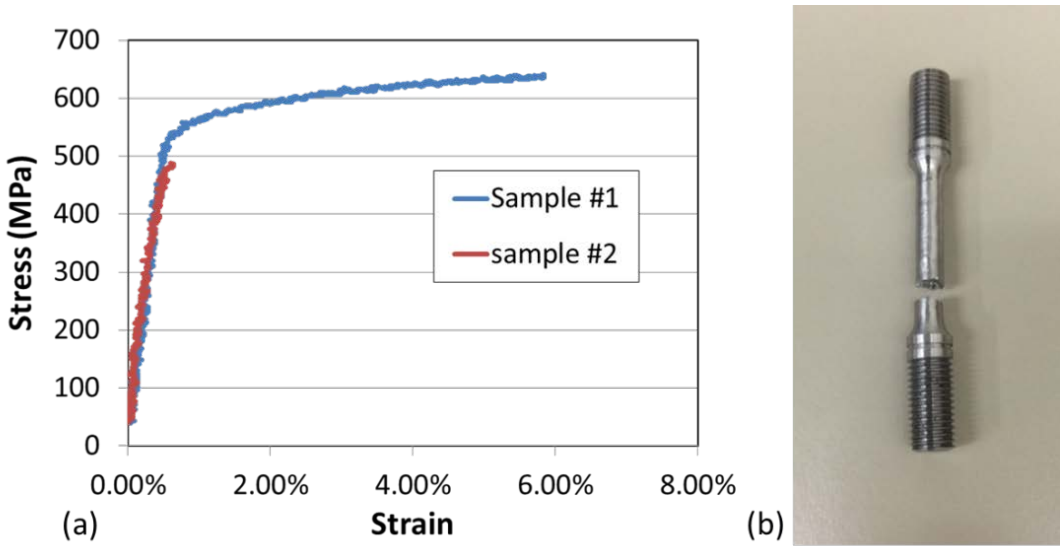

Figure 24 *Tensile test of the ferritic steel #2 after solutionization at 1200 °C for 8 h and aging at 600 °C for 12 h.*

3.g Oxidation test.

Small samples of Ferritic Steels #1 and #2 were prepared with dimensions close to 0.5”x0.5”x0.5”. All surfaces of the sample were ground to 1200 grit of SiC sand paper to remove all the surface imperfections. The samples were placed in Al_2O_3 crucibles which were then placed in the center of a tube furnace at 760 °C and 800 °C, respectively. Cyclic weight change of the samples was recorded per certain time interval. The weight change per unit volume is plotted in Figure 25.

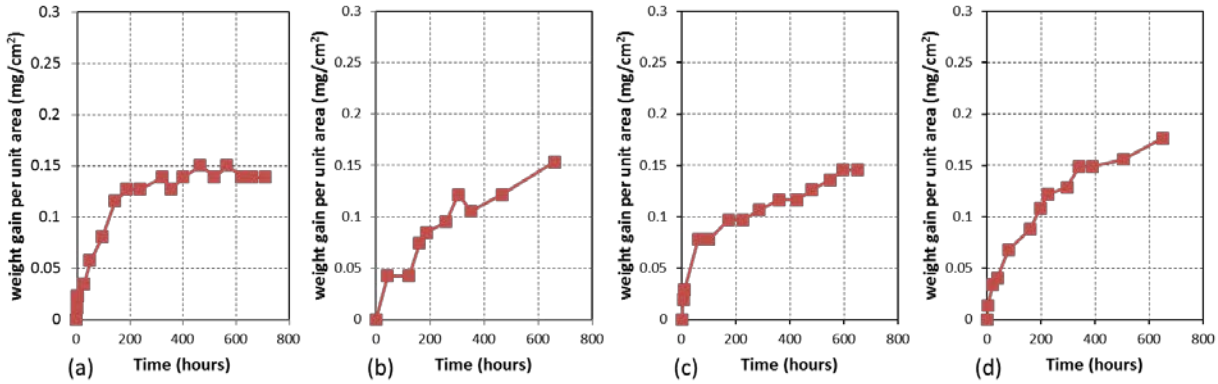

Figure 25 *Weight change per unit surface area of the two ferritic steels: (a) Ferritic Steel #1 oxidation at 760 °C; (b) Ferritic Steel #2 oxidation at 760 °C; (c) Ferritic Steel #1 oxidation at 800 °C; and (d) Ferritic Steel #2 oxidation at 800 °C.*

Both steels show very good oxidation resistance at both 760 °C and 800 °C. After an oxidation exposure at 800 °C for 650 h, the weight gain per unit area of the two steels is only ~0.15 mg/cm^2. The overall oxidation resistance of the steels is excellent and comparable to the state-of-the-art gas-turbine recuperator material NF709 (Fe-25Ni-20Cr base) [14], and to the alumina-forming austenitic (AFA) steels that were developed at the Oak Ridge National Laboratory (ORNL) [15].

After the oxidation exposures, the specimens were mounted in epoxy and cut in the middle. Metallography samples were prepared for both samples oxidized at 800 °C. Optical images taken at the interface between the steel and the epoxy are shown in Figure 26. No internal oxidation was found on both samples, and the results together with the excellent weight gain data indicate excellent oxidation resistance at 800 °C.

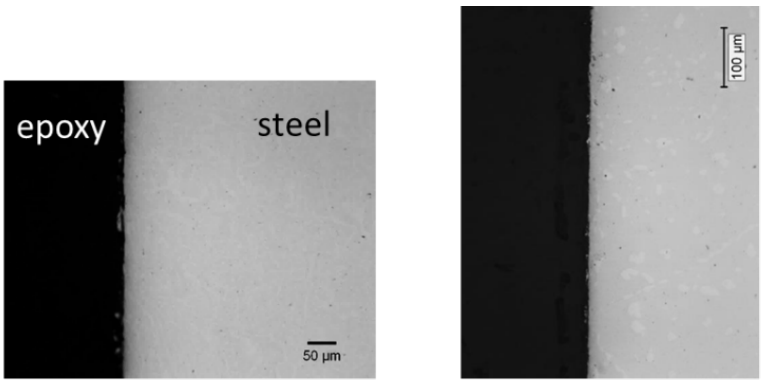

Figure 26 *Optical images of the two ferritic steels after oxidation test at 800 °C for 650 h.*

4. A new set of diffusion multiples design and fabrication to screen viable precipitates in the high-Mn austenitic steels.

4.a Diffusion multiple design and fabrication process.

One goal of this project is to develop high creep strength steels that can be operated for an extended period of time (e.g. 100,000 hours) at 760 ºC under very oxidative and corrosive environment of AUSC steam turbines and boilers. It is generally believed that austenitic steels with an fcc structure would be better for creep-rupture strength than ferritic steels. Most cost-effective elements for steels are ferrite stabilizers and only Mn and Ni are very effective austenite stabilizers. Mn is significantly cheaper than Ni and would be a great base element for high-temperature austenitic steels. However, a phenomenon called “blackening” was reported for high Mn alloys at high temperatures. We need to address this concern before spending significant efforts on high-Mn steels. Based on all the information we collected, we believe Mn is still a very worthwhile element to pursue and steels with both high Mn and high Cr are good candidates since Cr will afford the formation of a protective Cr_2O_3 to prevent the oxidation and

sublimation of Mn at high temperatures.

With Mn being selected as the key element and Ni being the next choice in stabilizing the austenitic phase, we have designed a diffusion multiple (Figure 27) to provide information on precipitate phases and phase diagrams of the following systems: Fe-Mn-Cr, Fe-Mn-Al, Fe-Mn-Ni, Fe-Mn-Mo, Fe-Mn-Nb, Fe-Ni-Al, Fe-Ni-Mo, Fe-Ni-Nb, Fe-Cr-Ni, Fe-Cr-Nb, Ni-Mn-Cr, Ni-Mn-Mo, Ni-Mn-Nb, Ni-Mo-Nb, Ni-Cr-Nb, Fe-Mn-Ni-Al, Fe-Mn-Nb-Al, Fe-Mn-Mo-Al, Fe-Mn-Cr-Al, Fe-Ni-Mo-Al, Fe-Ni-Cr-Al, and Fe-Ni-Nb-Al. We were able to combine two sets of diffusion multiples into one set by designing the diffusion multiple in a more condensed fashion than originally planned.

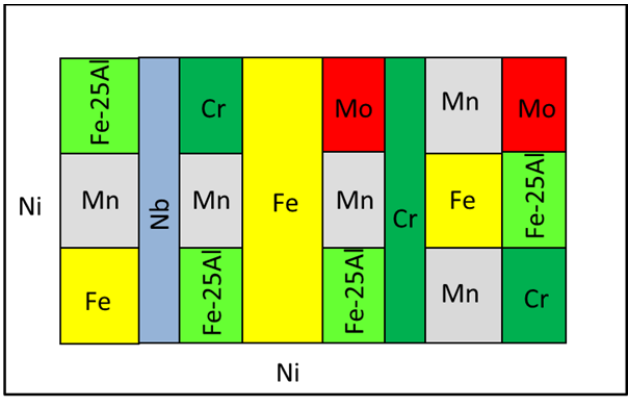

Figure 27 *The Fe-Mn-Cr-Nb-Ni-Mo-FeAl diffusion multiple designed for the current project to explore austenitic steels for AUSC boilers and steam turbines.*

The FeAl piece is a custom-made alloy with a composition of Fe-25wt.% Al. All the other elements are pure metals with purity greater than 99.9%. All the metal pieces were included in a pure Ni cartridge. The selection of Ni as the outer cartridge of diffusion multiples was due to the considerations of annealing temperature as well as its good weldability, comparable thermal expansion coefficient, and good mechanical strength at the annealing temperature. The thickness of the wall of the cartridge is 3 mm. The cartridge, the caps and all the inner metal pieces were carefully cut using electrical discharge machining (EDM) to the desired shapes and dimensions. The arrangement of the inner metal pieces was designed to include several ternary and quaternary materials systems that needed to be studied. The pieces were ground with SiC papers up to 1200 grit, and cleaned carefully in an ultrasonic cleaner with alcohol before putting inside the cartridge in a brick-laying pattern as shown in Figure 27. The Ni caps were attached on the top and bottom of the cartridge and vacuum electron-beam welding was performed to ensure that the cartridge was vacuum tight inside. HIP was executed at 1000 °C with an Ar pressure of 310 MPa for 8 h to squeeze the metal pieces to close contact against each other to allow the interdiffusion to take place.

Each diffusion multiple was encapsulated in a quartz-tube which was back filled with 1/5 atmospheric pressure of Ar (99.9% purity) and annealed at 1000 °C for 500 hours. The annealing temperature of 1000 °C was chosen to be high enough to induce wide solid solutions but still lower than the eutectic temperature of Ni-Mn which is only 1020 °C. A few Ta pieces were put

inside the quartz tube to act as oxygen getters during the annealing to minimize the oxygen contamination of the specimen. After annealing, the diffusion multiple was water quenched to room temperature to retain the high temperature phases that formed at 1000 °C to ambient temperature. Due to the high diffusion coefficients at high temperatures, considerable amount of interdiffusion and wide compositions of solid-solution phases were formed near the initial interfaces of the metal pieces. The whole fabrication process is summarized in Figure 28 and follows the general process of diffusion multiple making [16].

The quenched samples were cut to thin plates using EDM and careful metallography sample preparations were performed. Very wide diffusion zones were formed among the elements (especially in ferritic Fe) due to the relatively high diffusion kinetics at 1000 °C. When subjecting these diffusion multiples to a subsequent annealing at a lower temperature (e.g., 760 °C), various intermetallic precipitates were expected to grow out from the supersaturated matrix at different compositions.

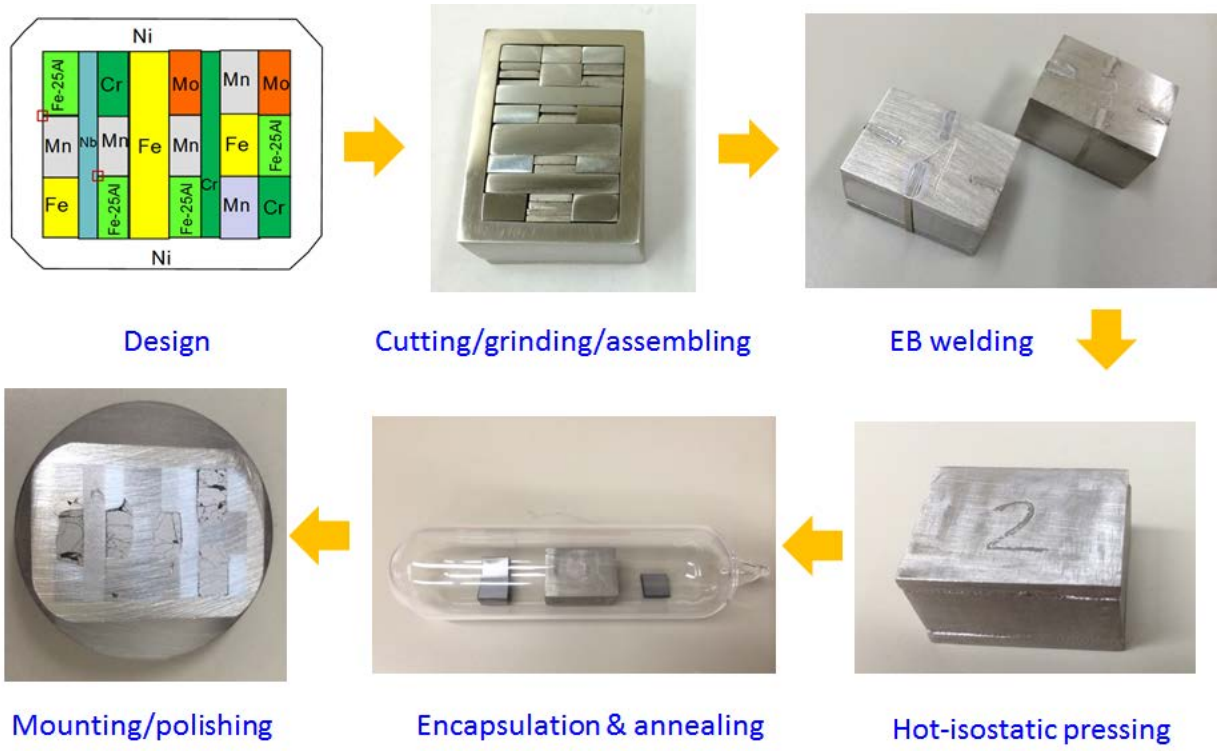

Figure 28 *Summary of the fabrication process of Fe-Mn-Cr-Nb-Ni-Mo-FeAl diffusion multiples.*

The first set of the diffusion multiple was unsuccessful due to the bad quality of the Mn pieces, which was claimed as “sputtering target” with a purity > 99.95% from the vendor of Atlantic Equipment Engineers. It is porous and trapped some gas inside. When subjecting to high temperature, the residual gas expanded and thus broke the welds between the cartridge and the caps. A second set of diffusion multiples was made using electrolytic pure Mn pieces and the diffusion multiples were successfully made.

4.b Phase equilibria of a few Fe-Mn and Fe-Ni related systems at 1000 °C.

The *Fe-Mn-Cr-Nb-Ni-Mo-FeAl* diffusion multiples were first annealed at 1000 °C for 500 h, followed by water quench. After careful metallography sample preparations, SEM images were taken on a few ternary/quaternary junctions. Composition analysis by electron probe microanalysis (EPMA) was performed across many phase interfaces to obtain the phase equilibria relationship among the ternary materials systems (especially the Mo-containing systems). The phase equilibrium data will be very useful to improve the current thermodynamic database to help design and development the Mn-containing high temperature steels. A few ternary systems were discussed in this report.

Fe-Ni-Mo

Several SEM images on the Fe-Ni-Mo tri-junction of the *Fe-Mn-Cr-Nb-Ni-Mo-FeAl* diffusion multiple were taken to form a montage to show the overall picture of the system with enough details, Figure 29(a). Then EPMA scan lines on the good locations along the phase boundaries were placed to get the composition profiles. The experimental data were plotted together and isothermal section phase diagram was constructed from the local phase equilibrium information. Figure 29(b) shows the comparison between the constructed phase diagram and the one from literature, showing good agreement.

Fe-Ni-Nb

Using a similar procedure as above, several SEM images were taken to form a montage of the Fe-Ni-Nb tri-junction, Figure 30. EPMA scan lines were carefully placed on the locations along the phase boundaries with proper lengths to capture the local equilibria. The local phase equilibrium information was plotted together to construct the isothermal section phase diagram, which is compared with literature phase diagram in Figure 30(b). Significant differences can be clearly seen and we believe our data are reliable and significant further work is required to complete the determination of this ternary system.

Fe-Cr-Mn

The EPMA data that we obtained are superimposed in Figure 31 (the black dots are the data points from this work) with all the available phase boundary data from literature. The lines are the calculated ternary phase diagram from Raynor (Inter. Mater. Rev. 1983). Most of the literature studies were focused on the Fe-rich bcc/fcc phase boundary, and the information on the other compositions in the phase diagram is very limited. The bcc/fcc phase boundary data obtained from the present work are in good agreement with the literature values.

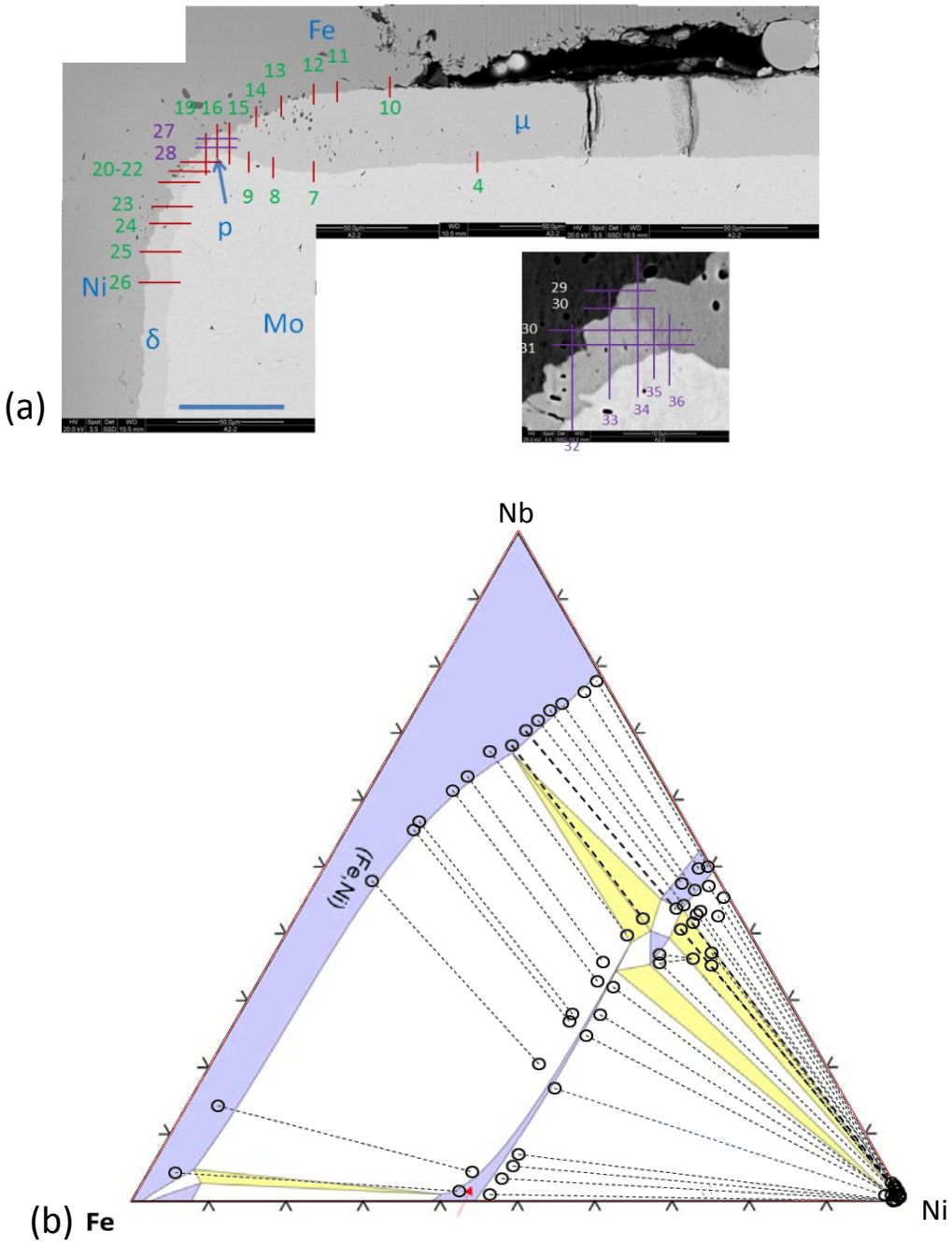

Figure 29 *(a) SEM image and EPMA scan locations of the Fe-Ni-Mo system; and (b) Constructed ternary phase diagram and comparison with literature result. The literature phase diagram was from Frisk K., Metall. Trans. A, 23 (1992) 639-649.*

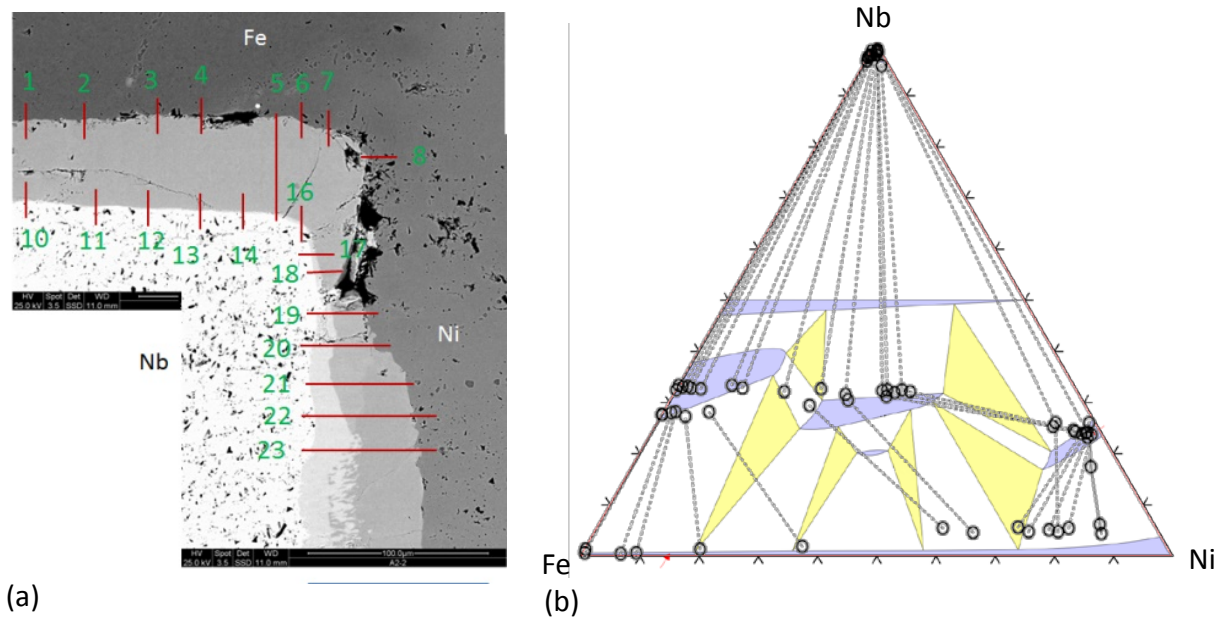

Figure 30 *(1) SEM images and EPMA plan of the Fe-Ni-Nb system. (2) The constructed ternary phase diagram and the comparison with literature. The literature phase diagram was from Raghavan V., Trans. Indian Inst. Met., 6B (1992) 1025-1027.*

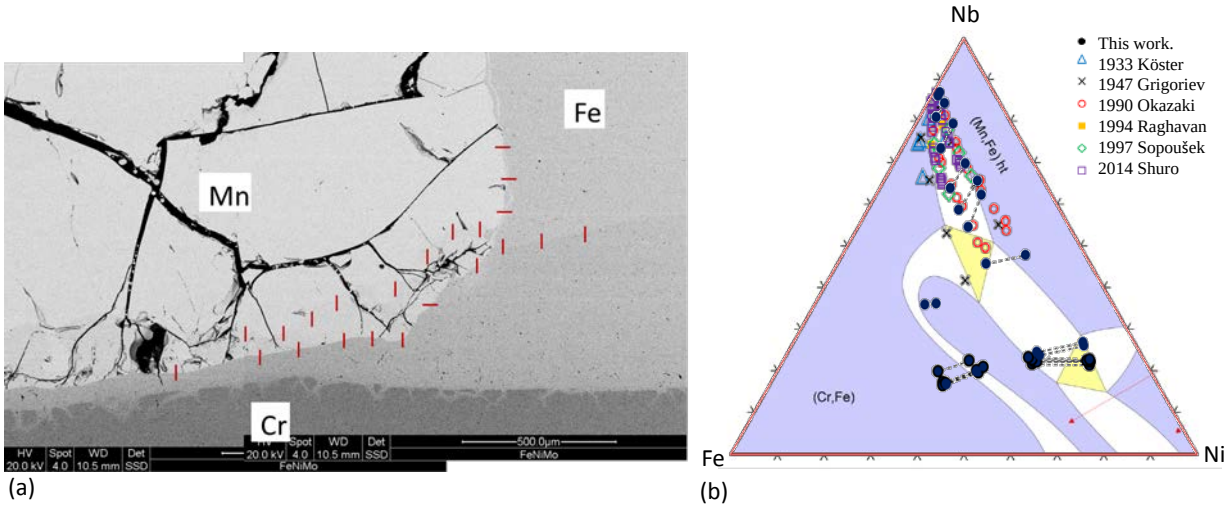

Figure 31 *Phase equilibria data of the ternary Fe-Cr-Mn system: (a) SEM image montage showing the Fe-Cr-Mn tri-junction together with the EPMA line scan locations; and (b) Experimental dataset obtained from the current diffusion multiple (black filled dots) in comparison with available literature values listed in the diagram.*

4.c Precipitation and microhardness tests of a few ternary and quaternary systems after dual-annealing at 760 °C for 200 h

In order to explore viable strengthening precipitates for austenitic steels that are potentially be used in 760 °C environment, we need first to let the precipitates grow at this temperature out from the supersaturated matrix which is created by annealing at 1000 °C for 500 h. We thus perform the second annealing of the diffusion multiple at 760 °C for 200 h. Several precipitates were found in the dual annealed diffusion multiple that was ground and polished for high-resolution SEM imaging and micro-hardness test.

An automatic micro-hardness tester was employed to perform the micro-hardness "mapping" on the dual-annealed diffusion multiple, which is highly efficient and saves significant amount of time. Annealing at 1000 °C for 500 h created large ranges of varying composition areas. During the annealing at 760 °C, relevant precipitates emerged from the supersaturated matrix at various locations/compositions (Figure 32), influencing the corresponding mechanical properties. The goal of microstructure imaging and microhardness mapping is to find the areas with finely precipitates but also with a proper volume fraction to yield desired strength without losing the toughness. Micro-hardness maps of the interesting ternary/quaternary junction provide key information to help design new austenitic steels. A few examples are shown here.

Fe-Cr-Mn tri-junction region

The load of the microhardness testing was chosen as 300 gram – constant load on the whole area. The spacing of the indents was 100 μm. From the hardness contour image (Figure 33) one can see that microhardness on pure Fe and Cr is low. In Fe-Cr binary diffusion zone, hardness is slightly increased due to the solid solution strengthening. While on the ternary junction containing Mn, the hardness increased significantly. This area might be just the intermetallic (Fe-Cr-Mn based ternary σ phase) or precipitates strengthened Fe-Mn solid solutions.

Fe-FeAl-Mn-Mo four-junction region

Following the similar process, the quaternary junction of Fe-FeAl-Mn-Mo was mapped as shown in Figure 34. Very fine precipitates were observed near the quaternary junction towards Mo (Figure 34). High-spatial resolution SEM and composition analysis need to be performed to investigate the precipitates and determine whether they could be used for the design of the new austenitic steels.

Ni-FeAl-Cr tri-junction region

The Ni-FeAl-Cr tri-junction results are shown in Figure 35. The high hardness region seems to be inside the FeAl-based intermetallic phase, thus not suited for further exploration for high temperature austenitic steels.

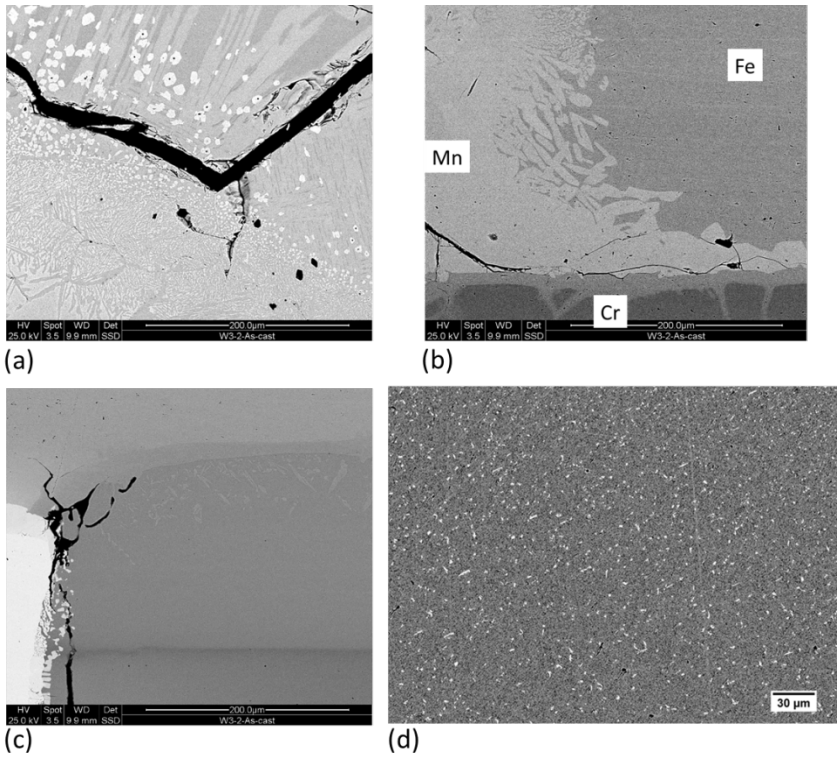

Figure 32 *Precipitates formed after the second annealing at 760 °C for 200 h: (a) Fe-Mn-Al-Mo; (b) Fe-Cr-Mn; (c) Fe-Ni-Al-Mo; and (d) Fe-Mn-Nb.*

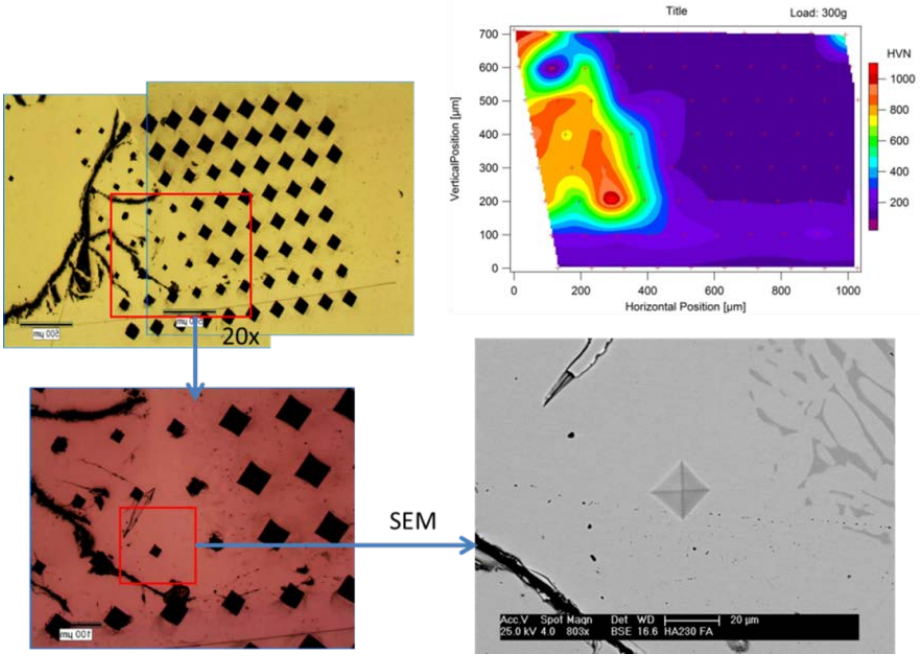

Figure 33 *Optical image of the microhardness mapped Fe-Cr-Mn tri-junction together with a microhardness contour map of the corresponding area. A higher magnification optical image and SEM image of the high-hardness location are also shown.*

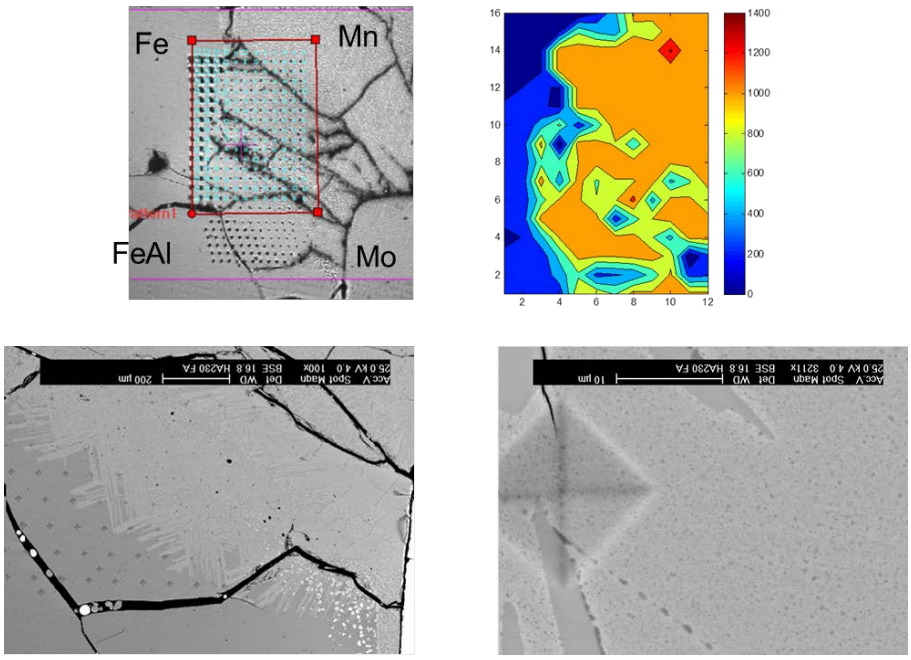

Figure 34 *Microhardness mapping on the Fe-FeAl-Mn-Mo quaternary junction showing the microhardness contour map of the corresponding area, the color code is on the right of the contour. High-resolution SEM images of the high-hardness locations with fine precipitates are also shown.*

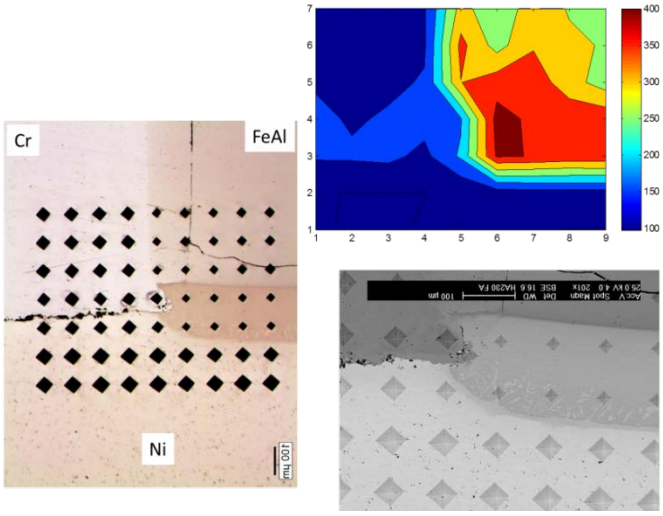

Figure 35 *Optical and SEM images of the micro indents mapped on the Ni-FeAl-Cr tri-junction and the corresponding microhardness contour map. The color code is on the right of the contour.*

5. Design of two new austenitic steels based on the intermetallic Laves phase.

5.a Alloying effects in the austenitic steels

Takeyama et al. [7] and Yamamoto et al. [17] have studied the fine precipitation morphology of the Laves phase, which could be employed to the design of novel high strength austenitic stainless steels. Laves-phase strengthened steel will be cost-effective, hot-corrosion resistant, with potentially good strength and creep resistance to be operated at 800 °C. We found fine precipitates in both Fe-Ni-Nb and Fe-Mn-Nb ternary systems, from the study of dual annealed diffusion multiples, Figure 36.

From the dual-anneal diffusion-multiple experiments, we identified the intermetallic Laves phase in the Fe-Mn-Nb and Fe-Ni-Nb systems as a viable strengthening phase since they are very finely distributed in the matrix of the austenitic phase. Based on this information, we designed our 1st austenitic steel using computational thermodynamics.

We carefully studied the alloying effect of each element on the phase equilibria at different temperatures since composition has a big effect on the resultant microstructure thus mechanical properties of the steels. Thermodynamic calculation software Thermo-Calc, with a steel database TCFe7, was used for this calculation. All the volume fractions and solvus temperatures of the intermetallic phases, such as, MC, $M_{23}C_6$, Laves, B2 (NiAl-based phase), sigma, and bcc could be calculated. The carbides, borides, and a phosphide (M_3P) were also included in the alloy to pin the grain boundaries during casting and forging. However, the volume fraction is usually low and it is also insensitive to the amount of Nb, Ni, Mn, and Al. To have a good oxidation resistance at the targeted temperature, enough Cr or Al should be present (usually > 13 wt%). Nb content is critical since it will have a significant effect on the volume fraction of the Laves phase. We took into account the results reported in literature that too high a content of Nb is bad for the creep resistance.

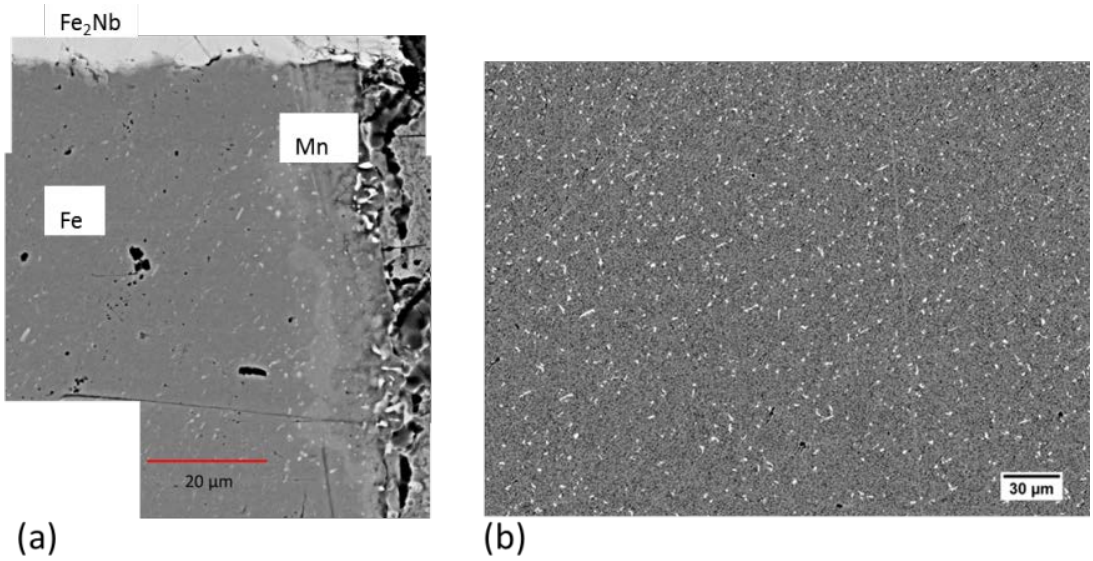

Figure 36 *SEM backscattered electron image montage of the Fe-Mn-Nb ternary junction where very finely dispersed Laves (Fe_2Nb) precipitates are distributed in the austenitic matrix, which is promising for the design of the new austenitic stainless steel. The white particles are the Laves phase.*

In particular, alloying effects of Al, Mn and Ni on the phase equilibria of this alloy were studied carefully using computational thermodynamics, as is shown in Figure 37. Solvus temperatures of the bcc and the sigma phases were computed and plotted as a function of composition to evaluate the stability of the austenitic phase and the detrimental sigma phase (no sigma phase should be present in the alloy at the temperature of long-term service). In order to achieve the desired austenitic matrix, the solvus temperatures of both phases need to be lower than the target temperature of 760 °C. Al is a very strong bcc stabilizer, but it is helpful to increase the oxidation resistance of the steel. When Al content is increased from 1 wt.% to 2 wt.%, the solvus temperature of the bcc phase increased from 585 °C to 773 °C. Mn is a good austenitic stabilizer which helps increase the stability of the austenitic phase, however it also promotes formation of the sigma phase. Ni is another good austenitic stabilizer which also helps inhibit formation of the sigma phase. However, Ni is expensive and for cost-reduction, we need to make a trade-off between Ni and Mn. We found from calculations that a balanced composition of 18 wt.% Ni, 4 wt.% Mn, and 1 wt.% Al is able to reduce the solvus temperatures of the bcc phase and the sigma phases to ~580 °C and 730 °C, respectively.

After balancing all the alloying effect of each element in the alloy, we determined the chemistry of the new austenitic steel strengthened by intermetallic Laves phase, Figure 38. The steel has been made at Metalwerks Inc. Another steel of the same basic composition, but with different minor content of Cu, was also ordered and received from Metalwerks and it is denoted as Austenitic Steel #2, Figure 39. Systematic tests of the mechanical properties were performed.

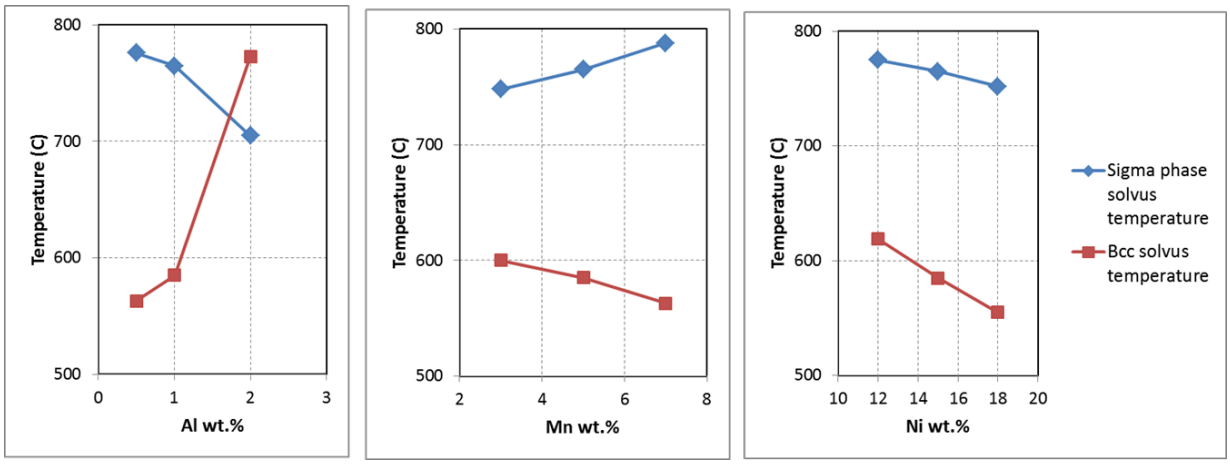

***Figure 37**. Alloying effect of Al, Mn, and Ni on the solvus temperatures of the bcc and the sigma phases in the Laves-strengthened austenitic steels.*

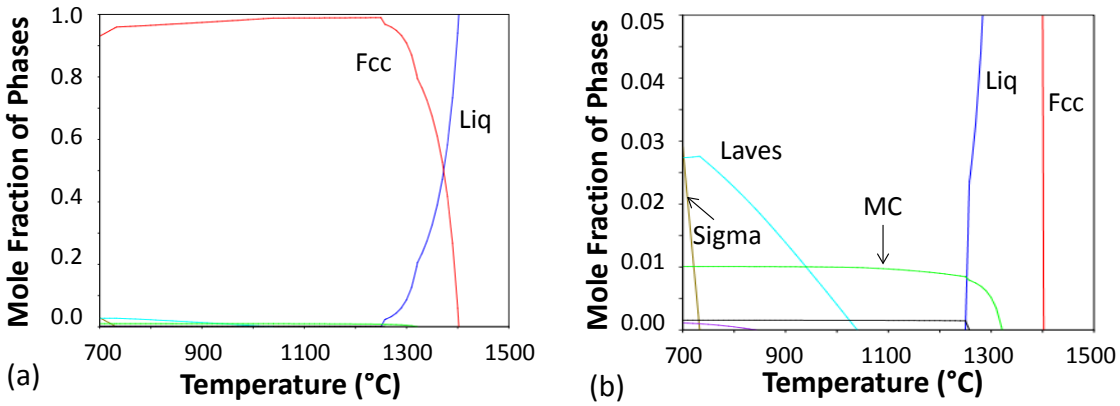

Figure 38 *Thermo-Calc calculation results of the new Austenitic Steel #1 (Composition is not shown – pending the intellectual property review at The Ohio State University. (b) shows the detail of low mole fraction phases).*

5.b Microstructure of the steel upon receiving, after solutioning, and after aging heat treatment.

Plates of two austenitic steels (#1 and #2) were received from Metalwerks Inc., as shown in Figure 39. Similarly to the ferritic steels, about 23 lb steel ingots were melted in vacuum, casted, and hammer forged to ~1 inch thick plates. The second austenitic steel (#2) has a different Cu composition from the first austenitic steel as mentioned before. Cu addition of an amount of 0.2%~0.5% usually improves the atmospheric corrosion resistance of the steel. Moreover, Cu is also an austenitic stabilizer, and promotes workability of the steel. Based on this fact, we designed the second austenitic steel with higher content (0.5 wt.%) of Cu.

The steel plate of Austenitic Steel #1 was cut into pieces, and metallography analysis was performed to investigate the microstructure of the steel, as shown in Figure 40. Clear eutectic structures were found in the specimen, which were formed during the solidification process. These eutectic microstructures need to be homogenized away before the precipitation studies. Considering the very similar compositions of the steels, homogenization heat treatment study was performed on only Austenitic Steel #1.

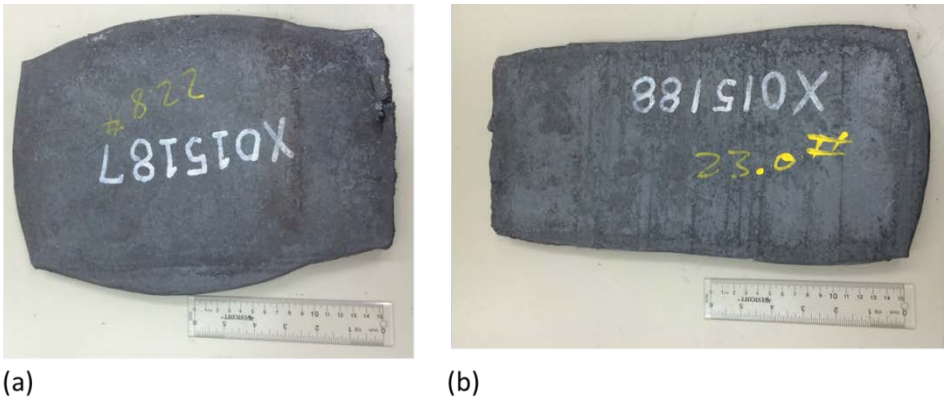

Figure 39 *Photos of the "as-received" austenitic steel #1 and #2 plates.*

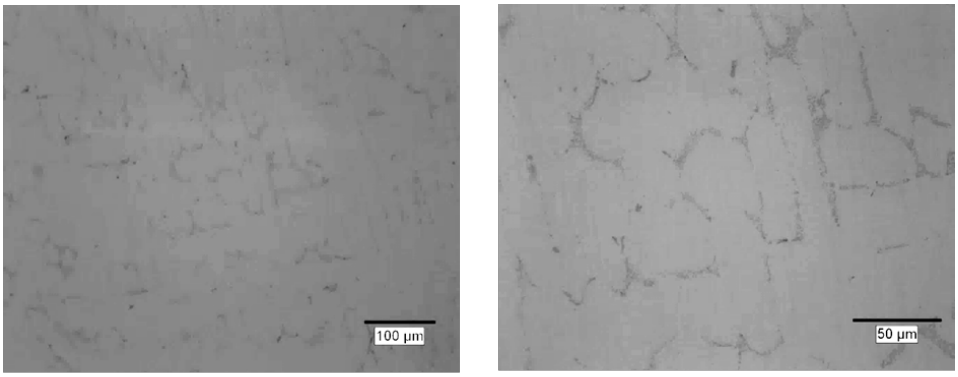

Figure 40 *Optical micrographs of the "as-received" austenitic steel #1: (a) and (b) are micrographs taken from the same steel specimen but with different magnifications.*

5.c Solid-solutioning heat treatment of Austenitic Steel #1

Various combinations of temperature and annealing time were carried out to find the optimal solutioning temperature and duration to dissolve the eutectic microstructures in the "as-received" steel. The initial trials of the solutioning were done with temperatures from 1150 °C to 1200 °C with 4 – 8 h of annealing durations, Figure 41. It was found that even after 8 hour solution annealing at 1200 °C, not all the eutectic microstructures were dissolved. The reason is attributed to the slow kinetics of some alloying elements such as Nb and W. Since a solution treatment at 1200 °C for 8 h is not enough to completely dissolve all the eutectic structures which were formed during the casting and thermomechanical processing. Further solutioning treatment of the steel was carried out at 1200 °C for 30 h and 50 h to examine whether longer annealing is enough to remove the eutectic structures. Since the oxidation of the steel might be a problem at 1200 °C, we encapsulated the steel in a quartz tube which was back filled with 1/5 atmospheric pressure of pure argon, before the long-term solid solutioning heat treatments. After the heat treatments, a small piece of the steel was cut and metallography analysis was performed to investigate the microstructure. Figures 42 and 43 are the optical images of Austenitic Steel #1 after being solutionized at 1200 °C for 30 and 50 h. No large Laves phase particles were observed, but some of the eutectic structures still remained after the solutioning. The eutectic structures might also be the carbides that were formed during the solutioning. Due to the large size and small volume fraction, we doubt the carbides will have a huge effect on the mechanical properties. Since the grain size of the steel is further controlled by the cold rolling after the solid solutioning, the solutioning heat treatment of the austenitic steels was selected to be 1200 °C for 50 h.

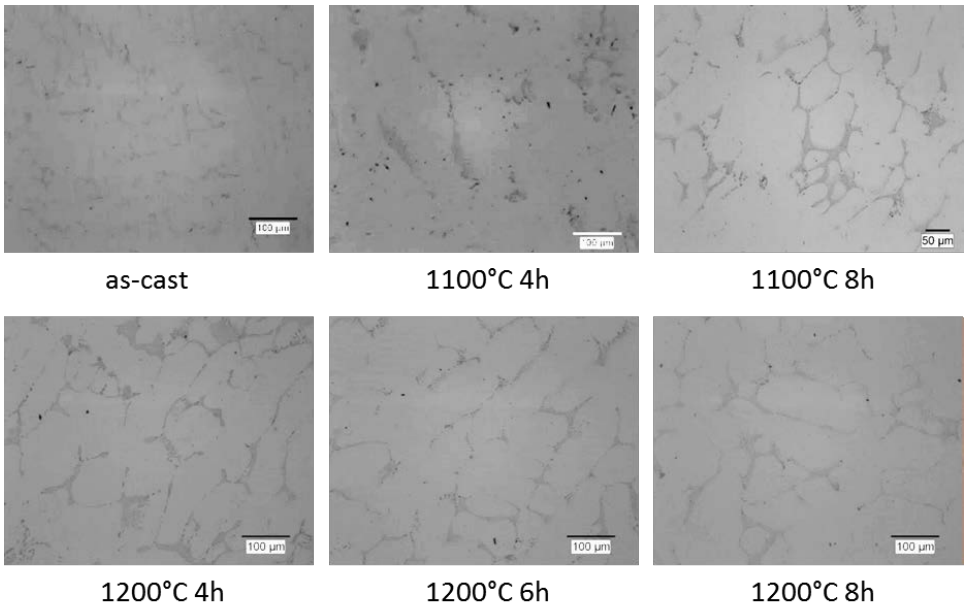

Figure 41 *Optical micrographs of Austenitic Steel #1 after solid solutioning with different temperatures and annealing durations.*

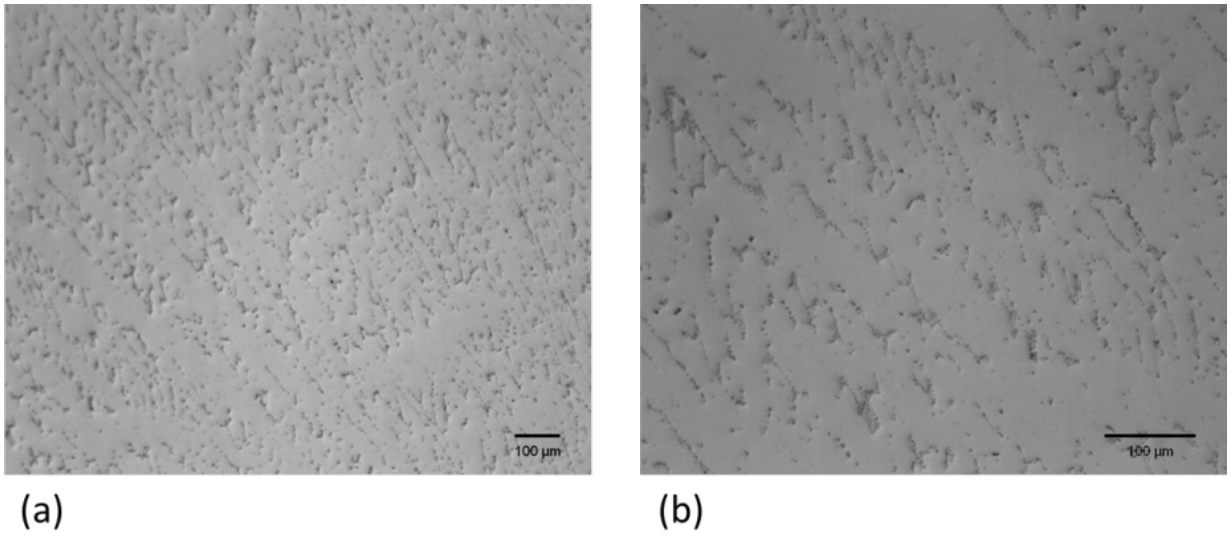

Figure 42 *Optical images showing the microstructure of Austenitic Steel #1 after solutioning treatment at 1200 °C for 30 h.*

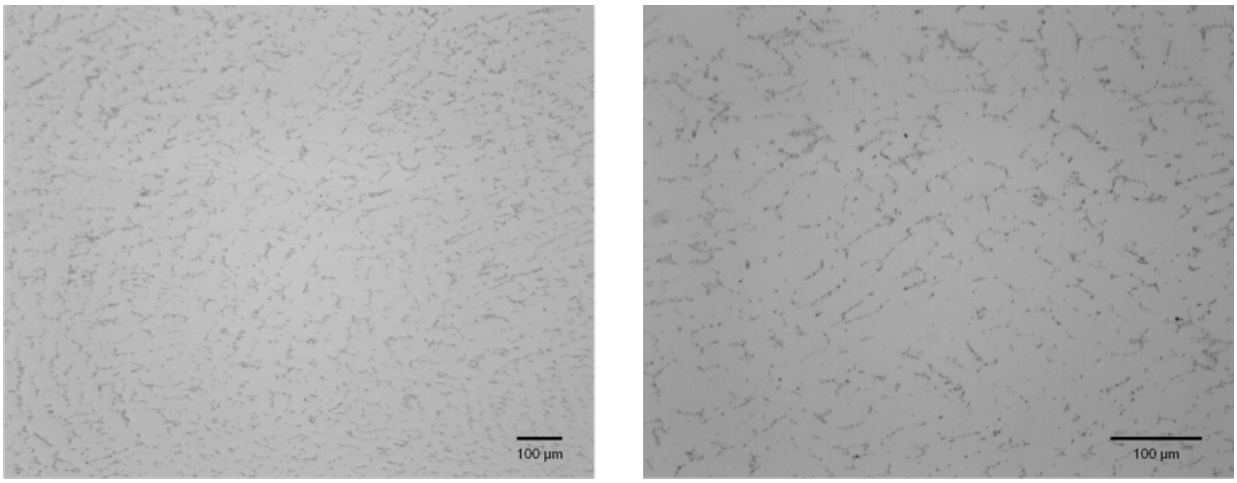

Figure 43 *Optical images showing the microstructure of Austenitic Steel #1 after solutioning treatment at 1200 °C for 50 h.*

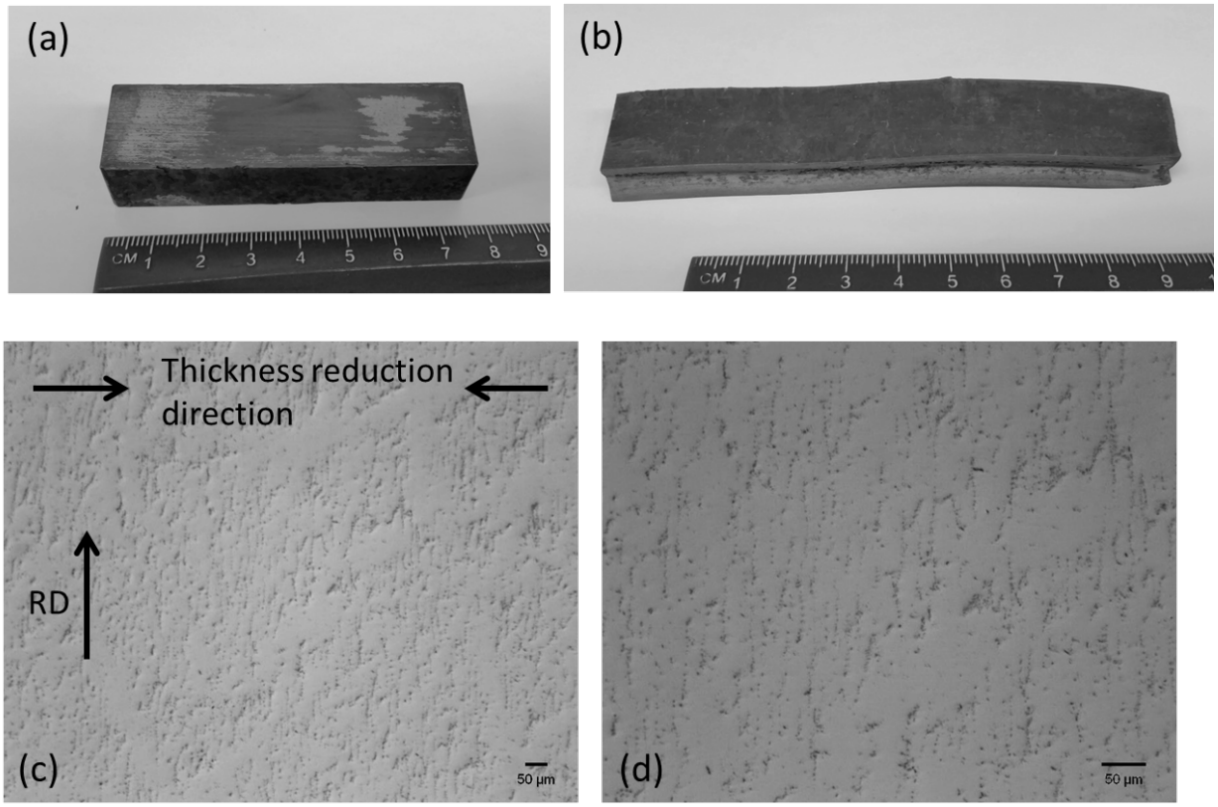

Figure 44 *(a) Steel after solutioning at 1200 °C for 30 h. (b) Cold-rolling on the steel bar with a 50% thickness reduction. (c-d) Optical images showing the microstructure of the steel.*

5.d Cold-rolling of the solutionized Austenitic Steel #1

After the solutioning treatment at 1200 °C for 50 h, significant grain growth took place, which degrades the toughness of the steel. Several previous studies showed the effect of the thermo-mechanical processing on the microstructure and thus the mechanical properties of steel. Cold-rolling introduces high density of dislocation which decreases the average grain size through recrystallization. The much increased dislocations also act as nucleation sites for fine NbC and the intermetallic Laves phase which also enhance the creep strength of the material. In this study, for Austenitic Steel #1, cold-rolling with a 50% thickness reduction was carried out after the solutioning process to enhance the mechanical property of the steel.

Figure 44 shows the microstructure change after the cold-rolling with a 50% thickness reduction. The grains are all oriented along the rolling direction.

Two separate steel bars were cut from the "as-received" steel plates of Austenitic Steels #1 and #2. They were first encapsulated in two quartz tubes and solutionized at 1200 °C for 50 h and then cold-rolling at ambient temperature for a 50% thickness reduction. It has been reported that cold-rolling was effective in controlling the grain size and refining the particle distribution of the strengthening precipitates [18]. The two steel bars were then aged at 800 °C for 100 h and water quench (one of the steel bar of Austenitic Steel #1 was aged at 760 °C for 200 h).

The resultant microstructures of the two steels were investigated using high-resolution SEM, Figure 45. The Laves phase (we anticipated it from Thermo-Calc^{TM} calculations, but further structural analysis of these phases need to be performed to confirm) is distributed quite evenly in the matrix for both Austenitic Steels #1 and #2. One can see that the microstructure of Austenitic Steel #1 annealed at 760 °C and 800 °C is very similar.

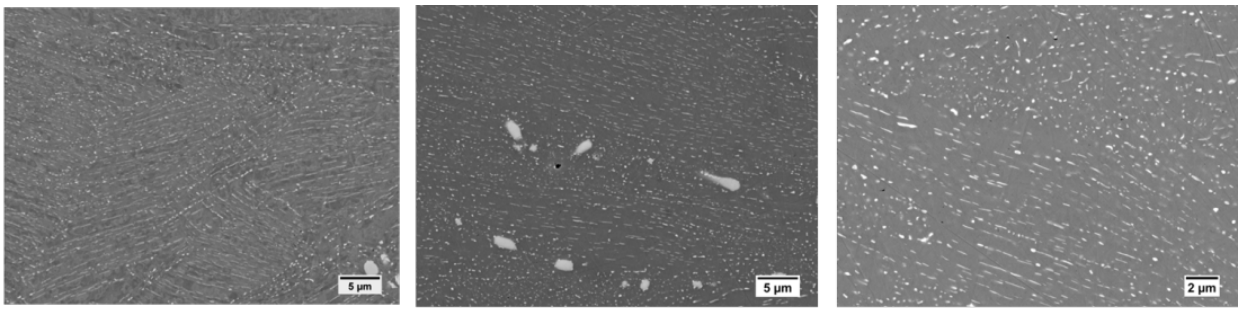

Figure 45 *High resolution SEM images showing the microstructures of the two austenitic steels after precipitation annealing.*

5.e Mechanical tests of the two austenitic steels.

After aging, the two steel bars were sent to the machine shop for tensile bar fabrication. The dimension of the tensile bars is with ASTM standard E8/E8M with 0.16 inch in diameter and 0.64 inch in length of the reduced section. Four round bars were made from each steel bar. Room temperature tensile test of the steel bar was conducted at OSU. Tensile test and creep test at

760 °C were conducted at Westmoreland Mechanical Testing & Research (WMT&R) company in Youngstown, PA.

The two steels show very similar strength and ductility at room temperature. The 0.2% yield strength of the steels is around 510 MPa. The ductility is around 30%. Both samples show obvious necking before failure, Figure 46.

The tensile tests at 760 °C were performed at the WMT&R company. The strain rate of the test was under ASTM E21 standard of 0.005in/in/min (mm/mm/min) through yield then 0.05in/in/min in displacement control through failure. Only the stress-strain curve with the strain is smaller than 0.7% was recorded as shown in Figure 47. The yield strength at this temperature is about 280 MPa. The total elongation of the two steels is ~57%.

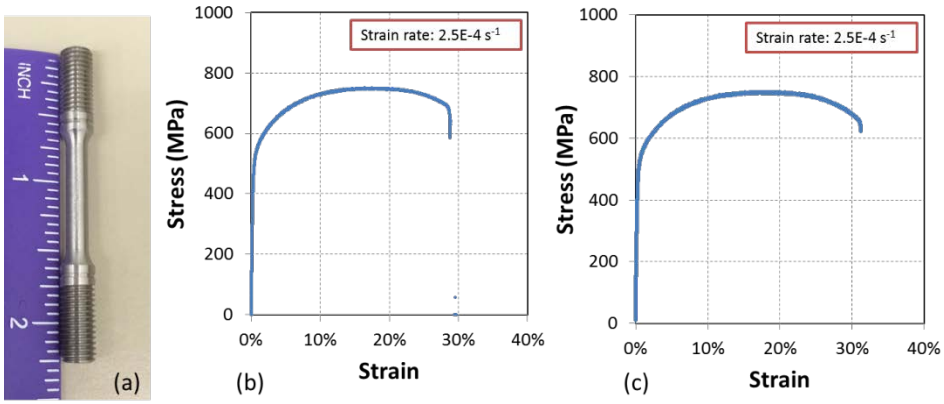

Figure 46 *Room temperature tensile test of Austenitic Steel #1 and #2, with a strain rate of $2.5x10^{-4}$ s^{-1}: (a) tensile specimen fabricated following ASTM standard E8/E8M; (b) Tensile test result of steel #1; and (c) Tensile test result of Austenitic Steel #2.*

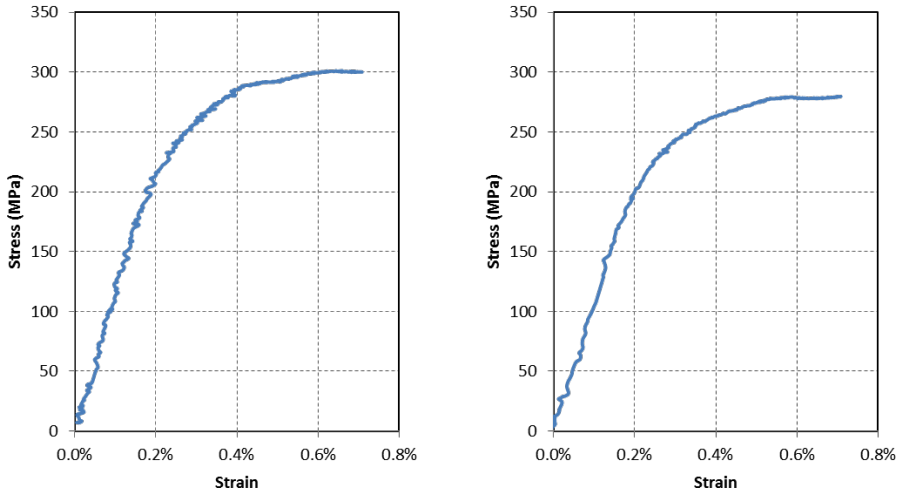

Figure 47 *Tensile test results of Austenitic Steels #1 and #2 at 760 °C.*

The creep test was also performed at the WMT&R Company. A total of 4 creep tests were performed and the results are reported in Figure 48. In Figure 48(a), the red line is Austenitic Steel #1 aged at 760 °C for 200 h with a test stress of 200 MPa; the blue line is Austenitic Steel #1 aged at 800 °C for 100 h with a test stress of 150 MPa; the green line is Austenitic Steel #2 aged at 800 °C for 100 h with a test stress of 150 MPa; the magenta line is Austenitic Steel #2 aged at 800 °C for 100 h with a test stress of 130 MPa. The calculated Larson-Miller parameters of the two steels were compared with the stainless steel 316 results from the literature. Our steels show better creep resistance than the traditional austenitic steels.

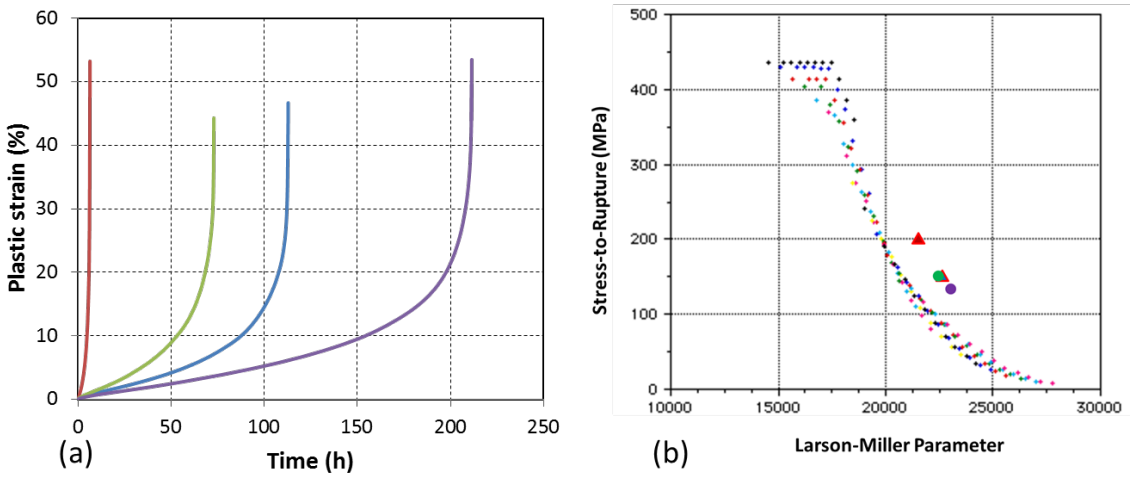

Figure 48 *Creep test of Austenitic Steels #1 and #2: (a) Stress to rupture curves of the austenitic steels tested at 760 °C, see text for details; and (b) calculated Larson-Millar parameter of the two steels in comparison with the traditional stainless steel 316. The triangles are Austenitic Steel #1, and filled dots are Austenitic Steel #2. The literature data of stainless steel 316 were from [19].*

5.f Oxidation test of the two austenitic steels.

Oxidation resistance tests were performed for the two austenitic steels exposed at 760 °C for up to 1200 h. Two small pieces of samples were cut from the steels and carefully ground with SiC sand papers down to 1200 grit to get rid of all the surface oxides and imperfections, as shown in Figure 49.

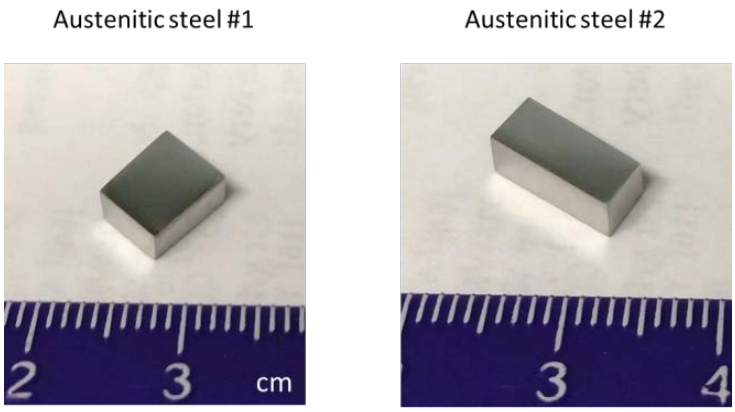

Figure 49 *Two small austenitic steel specimens prepared for the oxidation tests.*

These steel pieces were placed in alumina crucibles and at the center of a 760 °C tube furnace. Mass change of each specimen was recorded with a certain time interval. The mass change per unit surface area (mg/cm^2) as a function of time is plotted in Figure 50.

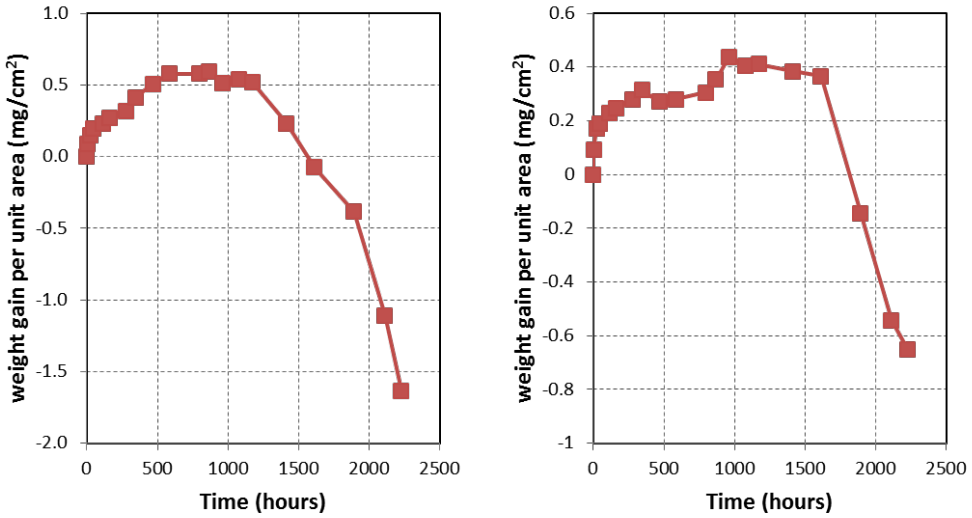

Figure 50 *Mass change as a function of time of Austenitic Steels #1 (left) and #2 (right) during the oxidation tests at 760 °C.*

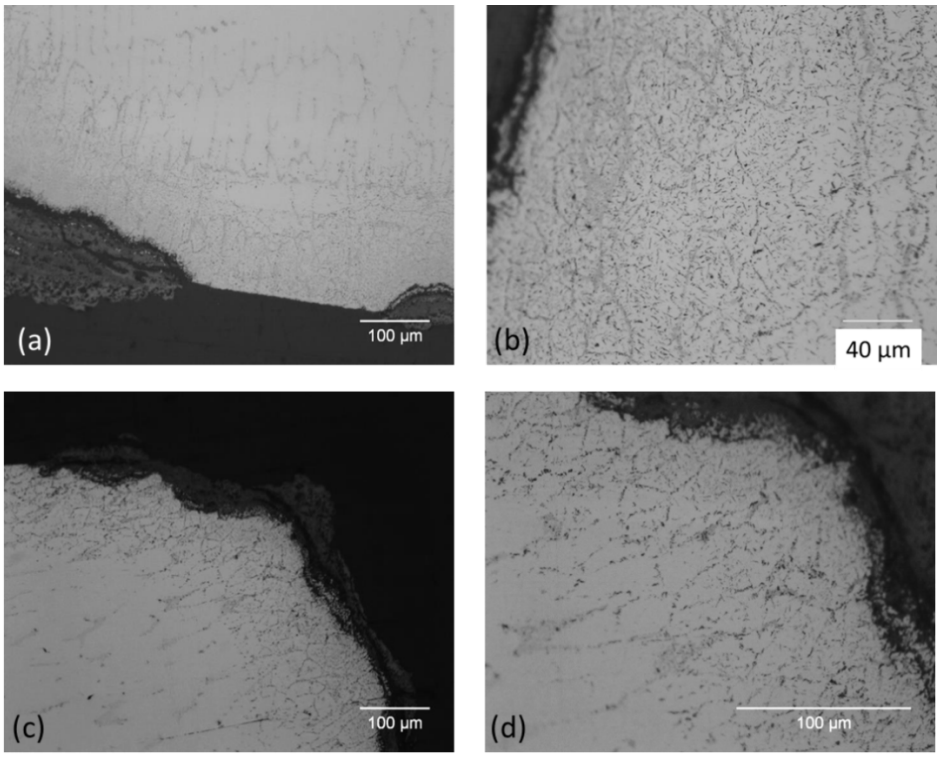

Figure 51 *Optical images of the two austenitic steels after oxidation tests: (a) and (b) Austenitic Steel #1 with different magnifications; and (c) and (d) Austenitic Steel #2 with different magnifications.*

Figure 50 shows the mass change of Austenitic Steels #1 and #2 as a function of time during the oxidation tests. Both specimens have been exposed at 760 °C for ~2200 hours. The weight gain of the two specimens was only ~0.5 mg/cm^2 before the surface began to flake off. The weight gain was slightly worse than the two ferritic steels probably due to the lower content of Cr, but still comparable to the state-of-the-art heat resistant steels [14,15]. The weight change curves start to sharply decrease after ~1200 hours, which was due to the oxides flaking off from the surface. Between the two austenitic steels, Austenitic steel #2 shows slightly better oxidation resistance due to the slightly higher content of Cu addition which increases the atmospheric corrosion resistance of the steel.

The microstructure near the surface was examined under optical microscopy after the oxidation tests to see if there was any internal oxidation. The two specimens were mounted in epoxy and ground and polished. Optical images with different magnification were taken and shown in Figure 51. Slight internal oxidation was observed in the two steels after exposing at 760 °C for 2200 h, especially some oxidation of the fine carbide particles and/or the Laves phase particles along the grain boundaries and within the grains near the surface. A few large oxide nodules are observed, indicating non-uniform oxidation. Composition or microstructure inhomogeneity may be the culprit. Nevertheless, it is clear that the oxidation resistance of the austenitic steels (Figures 50 and 51) are not as good as the ferritic steels (Figures 25 and 26). Even though the oxidation tests did not run to 2200 h at 760 °C for the ferritic steels, the test at 800 °C for 650 h would be as aggressive as the test performed at 760 °C for 2200 h. The two austenitic steels can be used at 760 °C for up to 1000 h (for Austenitic Steel #1) and 1500 h (for Austenitic Steel #2) before significant oxidation spallation.

6. Summary and concluding remarks.

One key objective of this project was to demonstrate a high-throughput methodology for the design and development of new alloys. The methodology consisted of: 1) employing a dual-anneal diffusion-multiple approach to rapidly screen for viable strengthening phases for high temperature steels aiming for applications in advanced ultrasupercritical steam turbines; 2) using computational thermodynamics to design new alloys based on the discovery of viable strengthening phases from diffusion multiples in order to achieve property balance through the use of multicomponent compositions as well as additional phases; and 3) experimentally testing the properties of the designed alloys to validate and improve the properties of the alloys. We validated this effective approach through two sets of systems based on either a ferritic base or an austenitic base. The intermetallic Chi phase was identified as a viable strengthening phase for the Fe-Cr-Mo based ferritic steels, and the Laves phase was found to be effective as a strengthening phase for Mn-containing austenitic steels. Even though the creep properties of the alloys are only comparable to or inferior to the current state of the art alloys, considering the fact that only two alloys were tested for each class of steels during this project, the results are very encouraging since every new class of alloys takes considerable number of years to mature.

Two ferritic steels were designed, made and tested, based on the intermetallic Chi phase found in the Fe-Cr-Mo-Co-Ni dual-annealed diffusion multiple. The two ferritic steels designed using computational thermodynamics showed excellent oxidation resistance and good creep resistance at high temperatures, considering their ferritic bases. However, the two steels showed brittleness and sample to sample variability in ductility. The reasons for the low ductility might include: 1) the macro segregation during the solidification process especially for the heavy elements such as Mo and Nb in the steel; 2) the large grain size found in the steel after the solid solution heat treatment; and 3) the hammer forging process used to upset the steel ingots to 1-inch thickness plates (might be too rough for these steels). We believe there is no inherent brittleness based on the chemistries of the steels and the Chi phase strengthened steels are still a promising new direction for further exploration.

A Fe-Mn-Cr-Nb-Ni-Mo-FeAl diffusion multiple set with Mn and Ni as the major austenite stabilizers was designed and fabricated to screen for viable strengthening precipitates in the austenitic matrix at high temperatures. Elements such as Cr and Al were included in this diffusion multiple set to make sure the compositions include these elements for oxidation resistance. Key potential alloying elements such as Mo and Nb are also included for their strengthening potential. The diffusion multiple was first annealed at 1000 °C for 500 h to create a large range of solid solution compositions through interdiffusion. A second anneal of the diffusion multiple at 760 °C for 200 h induces various precipitates. There was insufficient funding to complete the screening of all the ternary and higher order systems contained in the diffusion multiple: Fe-Mn-Cr, Fe-Mn-Al, Fe-Mn-Ni, Fe-Mn-Mo, Fe-Mn-Nb, Fe-Ni-Al, Fe-Ni-Mo, Fe-Ni-Nb, Fe-Cr-Ni, Fe-Cr-Nb, Ni-Mn-Cr, Ni-Mn-Mo, Ni-Mn-Nb, Ni-Mo-Nb, Ni-Cr-Nb, Fe-Mn-Ni-Al, Fe-Mn-Nb-Al, Fe-Mn-Mo-Al, Fe-Mn-Cr-Al, Fe-Ni-Mo-Al, Fe-Ni-Cr-Al, and Fe-Ni-Nb-Al (Note: not all of the systems were available due to cracking and porosity in the diffusion multiple sample). The intermetallic Laves phase was identified in the Fe-Mn-Nb or Fe-Ni-Nb ternary system as a viable strengthening precipitate at 760 °C for austenitic steels, which is similar to the finding of Takeyama through years of experiments. Such finding was based on both microstructure examination and microhardness mapping.

A few isothermal sections of the Fe-Mn or Fe-Ni related ternary phase diagrams were

established which will serve as important input to future thermodynamic assessments to improve the thermodynamic databases for a more accurate prediction in the alloy design process.

Two austenitic steels based on the intermetallic Laves phase in the Fe-Mn(Ni)-Nb system were designed using computational thermodynamics. Extensive parametric optimization studies were performed using Thermo-Calc^{TM} to determine the optimal compositions of the two steels. The two designed steel compositions were induction melted and then hammer forged to 1-inch thickness plates (~23 lb each). Solution heat treatment and precipitation heat treatment were optimized and performed. Specimens for tensile, creep and oxidation resistance were made and tested. The two steels were found to have good to excellent oxidation resistance (inferior to the ferritic steels developed in this project). The Larson-Miller parameter of these two austenitic steels are very similar and both steels have better creep resistance than the traditional 316 stainless steels, but not as good as the creep resistance of the alumina forming alloys (AFAs) developed at ORNL [14,15].

During the research of this project, we developed an elegant and easy-to-implement gradient temperature heat treatment process for effective study of phase precipitation as shown in Figures 6 to 10. This process can be used by essentially any laboratories without requiring expensive equipment – a tube furnace, a set of thermocouples, and a thermocouple temperature reader are all that required. The process is extremely effective as demonstrated in Figures 6 to 10.

7. Publications, patents and presentations.

1. Ji-Cheng Zhao: “High temperature steels and articles made thereof”, OSU patent disclosure, filed in April 2013. (Not filed for patent yet due to the fact that the properties of steels do not show sufficient benefits in comparison to the current state of the art)
2. Changdong Wei and Ji-Cheng Zhao: “Efficient study of precipitation using gradient temperature heat treatment for the development of high-temperature Fe-Cr-Mo ferritic steels”, Manuscript in final preparation
3. Changdong Wei and Ji-Cheng Zhao: “Development of Fe-Cr-Mo based Chi phase strengthened ferritic steels”, Manuscript in preparation
4. Changdong Wei and Ji-Cheng Zhao: “Phase equilibria in the Fe-Mo-Ni, Fe-Nb-Ni, and Fe-Cr-Mn systems at 1000 °C”, Manuscript in preparation
5. Changdong Wei and Ji-Cheng Zhao: “Mn-containing austenitic steels strengthened with a Laves phase”, Manuscript in preparation
6. Changdong Wei and Ji-Cheng Zhao: “Studies of Fe-Mn-X systems for the development of high-temperature austenitic steels”, (Oral presentation) Materials Science and Technology 2015 (MS&T 2015), Columbus, Ohio, October 4-8, 2015.
7. Changdong Wei, Qiaofu Zhang, Siwei Cao, and Ji-Cheng Zhao: “High-throughput study of phase transformations and microstructure evolution using diffusion experiments”, (Oral presentation) The Third World Congress on Integrated Computational Materials Engineering (ICME 2015), Colorado Springs, Colorado, USA, June 1 – June 4, 2015.
8. Changdong Wei*, Siwei Cao, and Ji-Cheng Zhao: “Effective exploration of novel high-temperature steels for advanced ultrasupercritical steam turbines” (Invited talk) TMS Annual Meeting 2015, Orlando, Florida, March 15-19, 2015.

9. Changdong Wei and Ji-Cheng Zhao: “Study of Fe-Mn-X systems for the development of high-temperature steels for advanced ultrasupercritical steam turbines”, (Oral Presentation) Materials Science & Technology 2014 (*MS&T 14*), Pittsburgh, PA, October 12-16, 2014.
10. Changdong Wei and Ji-Cheng Zhao: "Effective exploration of new 760 °C capability steels for coal energy." (Oral presentation) National Energy Technology Laboratory (NETL) Crosscutting Research Review Meeting, Pittsburgh, PA, May 19-23, 2014.
11. Siwei Cao, Changdong Wei, and Ji-Cheng Zhao: “Development of high-temperature steels for advanced ultrasupercritical steam turbines”, (Invited talk) TMS Annual Meeting, San Diego, CA, February 16-20, 2014.

Reference

[1] L. Jiang, Y. Chen, T. Hanlon, A. Loghin, C. Shen, R. Schwant, and J. Li, Modeling Creep-Fatigue-Environment Interactions in Steam Turbine Rotor Materials for Advanced Ultrasupercritical Coal Power Plants, Conference Proceedings of the 25th Annual Conference on Fossil Energy Materials, April 26-28, 2011, NETL, DOE: http://www.netl.doe.gov/publications/proceedings/11/fem/presentations/Modeling-Creep-Fatigue_Jiang.pdf (Accessed November 2011).

[2] R. Viswanathan, R. Purgert, S. Goodstine, J. Tanzosh, G. Stanko, J.P. Shingledecker, and B. Vitalis, U.S. Program on Materials Technology for Ultrasupercritical Coal-Fired Boilers, Advances in Materials Technology for Fossil Power Plants: Proceedings of the 5th International Conference, Paper #05226G, ASM International, 2008.

[3] R. Viswanathan and W. Bakker, J. Mater. Eng. Perfor., 10 (2001) 81-95.

[4] R. Viswanathan and W. Bakker, J. Mater. Eng. Perfor., 10 (2001) 96-101.

[5] R. Viswanathan, J.F. Henry, J. Tanzosh, G. Stanko, J. Shingledecker, B. Vitalis, and R. Purgert, J. Mater. Eng. Perfor., 14 (2005) 281-292.

[6] R. Viswanathan, J. Sarver, and J.M. Tanzosh, J. Mater. Eng. Perfor., 15 (2006) 255-274.

[7] S. Ishikawa, T. Matsuo, and M. Takeyama, Mater. Res. Soc. Symp. Proc., 980 (2007) 0980-II05-17.

[8] Y. Hasebe, K. Hashimoto, T. Matsuo, and M. Takeyama, Mater. Res. Soc. Symp. Proc., 1295 (2011) 171-176.

[9] I. Tarigan, K. Kurata, N. Takata, T. Matsuo, and M. Takeyama, Mater. Res. Soc. Symp. Proc., 1295 (2011) 317-322.

[10] J.-C. Zhao, M. Larsen, and V. Ravikumar, Mater. Sci. Eng. A., 293 (2000) 112-119.

[11] S. Cao, J.-C. Zhao, Acta Mater., 88 (2015) 196-206.

[12] S. S. Ordanyan, E. K. Stepanenko, Inorg. Mater., 13 (1977) 312.

[13] J. S. Kasper, Acta Metall., 2 (1954) 456.

[14] Y. Yamamoto, M. P. Brady, Z. P. Lu, P. J. Maziasz, C. T. Liu, B. A. Pint, K. L. More, H. M. Meyer, E. A. Payzant, Science, 316 (2007) 433-436.

[15] M. P. Brady, Y. Yamamoto, M. L. Santella, P. J. Maziasz, B. A. Pint, C. T. Liu, Z. P. Lu, H. Bei, JOM, 60 (2008) 12-18.

[16] J.-C. Zhao, in: J.-C. Zhao (Ed.), Methods for Phase Diagram Determination, Elsevier Ltd, Oxford, 2007, Chapter 7.

[17] Y. Yamamoto, M.P. Brady , Z.P. Lu, C.T. Liu, M. Takeyama, P.J. Maziasz, B.A. Pint, Metall. Mater. Trans. A, 38A (2007) 2737.

[18] B. Hu, G. Trotter, Ian Baker, M.K. Miller, L. Yao, S. Chen, Z. Cai, Metall. Mater. Trans. A, 46A (2015) 3773.

[19] ASME Code Cases : Nuclear Components. Case N-47-30, Section III, Division 1. 1992 ASME Boiler and Pressure Vessel Code.